LUND UNIVERSITY

Diffusion-encoded MRI for assessment of structure and microcirculation

Aspects of q-space imaging and improved IVIM modelling

Scherman Rydhög, Anna

2017

Diffusion-encoded MRI for assessment of structure and microcirculation:
Aspects of *q*-space imaging and improved IVIM modelling

Diffusion-encoded MRI for assessment of structure and microcirculation

Aspects of *q*-space imaging and improved IVIM modelling

Anna Scherman Rydhög

LUND
UNIVERSITY

Thesis for the degree of Doctor of Philosophy
Thesis advisors: Associate Professor Linda Knutsson (main supervisor),
Professor Ronnie Wirestam and Professor Freddy Ståhlberg
Faculty opponent: Associate Professor Göran Starck, Department of Radiation Physics at the Institute of Clinical Sciences, University of Gothenburg, Gothenburg, Sweden.

To be presented, with the permission of the Faculty of Science of Lund University, for public criticism in Demonstration Room 10, Department of Medical Imaging and Physiology, Main Building, Level IV, Skåne University Hospital, Lund, on Friday the 15th of December at 9.00

Organization
LUND UNIVERSITY

Dept. of Medical Radiation Physics
Skåne University Hospital, Lund

SE-221 58 Lund, Sweden

Author(s)
Anna Scherman Rydhög

Document name
Doctoral Thesis

Date of issue
2017-12-15

Sponsoring organization

Title and subtitle
Diffusion-encoded MRI for assessment of structure and microcirculation:
Aspects of *q*-space imaging and improved IVIM modelling

Abstract
Diffusion and perfusion MRI are valuable methods for investigating the microstructure and viability of tissue. One pure diffusion study was included in this thesis, with the purpose of studying microstructure and carrying out size estimations with the *q*-space diffusion imaging method. This is a method that has predominantly been explored with NMR spectrometers. In our study, a biological phantom consisting of asparagus stems was investigated using a clinical MRI unit to gain further knowledge about the *q*-space methodology in a setting where gradient performance is limited. Although the *q*-space method showed limited possibilities, retrieval of some structural information was shown to be feasible.

In the remaining three doctoral thesis projects, the intravoxel incoherent motion (IVIM) imaging concept was explored, allowing for extraction of combined diffusion and perfusion information from a given dataset. IVIM imaging is a non-invasive technique for acquiring diffusivity as well as microvascular and perfusion-related parameters using a diffusion-weighted pulse sequence. The model used in this technique is often limited because no relaxation properties are incorporated, and also because the signal component from blood is contaminated by cerebrospinal fluid/free water.

One study was dedicated to exploring the IVIM parameters at different field strengths and the influence of relaxation and signal-to-noise ratio (SNR) was observed. Although the repeatability was generally better at higher magnetic field strength, it was shown that the relaxation properties and an unexpectedly low SNR at high field strengths resulted in erroneous blood volume estimates. The model commonly used for IVIM data analysis was then modified to compensate for relaxation effects, based on literature values. When this correction was performed, results from the lower field strengths showed lower discrepancy from expected values, while the results from higher field strength were still erroneous, likely due to physiological noise.

In a following project, relaxation times were actually measured during the data collection, and incorporated to compensate for relaxation and improve the fitting procedure. The model was also upgraded to a three-compartment model to better describe the underlying tissue by including the cerebrospinal fluid component. Compared to a non-relaxation-compensated model, the three-compartment model with relaxation-compensated data modified the obtained results and reduced the CSF contamination.

The last IVIM project also included a three-compartment model, but in this case the purpose of the third compartment was to improve the quantification of the fraction of free water. The free water fraction has been established as a source of clinically useful image contrast, pointing at pathologies that affect the extracellular space, for example, atrophy and neuroinflammation. With our model, the bias from microcirculation was reduced in the free water estimate. A model where extracellular and microvascular effects can be separated might enable new diagnostic possibilities.

Key words

Classification system and/or index terms (if any)

Supplementary bibliographical information

Language
English

ISSN and key title

ISBN 978-91-7753-481-5 (print)
978-91-7753-481-5 (pdf)

Recipient's notes

Number of pages 120

Price

Security classification

Signature

Date 2017-11-06

Diffusion-encoded MRI for studies of structure and microcirculation

Aspects of *q*-space imaging and improved IVIM modelling

Anna Scherman Rydhög

LUND
UNIVERSITY

Coverphoto by Kyle Bean (BlinkArt)

Funding information: The thesis work was financially supported by the Swedish Research Council, the Swedish Cancer Society, the Crafoord foundation and the Lund University Hospital Donation Funds.

Faculty of Science, Department of Medical Radiation Physics

ISBN 978-91-7753-481-5 (print)

ISBN 978-91-7753-481-5 (pdf)

Printed in Sweden by Media-Tryck, Lund University
Lund 2017

"I cannot be right all the time. Quite often I is left instead of right."
– Roald Dahl, The BFG

Table of Contents

Summary

Diffusion and perfusion MRI are valuable methods for investigating the microstructure and viability of tissue. One pure diffusion study was included in this thesis, with the purpose of studying microstructure and carrying out size estimations with the q-space diffusion imaging method. This is a method that has predominantly been explored with NMR spectrometers. In our study, a biological phantom consisting of asparagus stems was investigated using a clinical MRI unit to gain further knowledge about the *q*-space methodology in a setting where gradient performance is limited. Even though the *q*-space method showed limited possibilities, retrieval of some structural information was shown to be feasible.

In the remaining three doctoral thesis projects, the intravoxel incoherent motion (IVIM) imaging concept was explored, allowing for extraction of combined diffusion and perfusion information from a given dataset. IVIM imaging is a non-invasive technique for acquiring diffusivity as well as microvascular and perfusion-related parameters using a diffusion-weighted pulse sequence. The model used in this technique is often limited because no relaxation properties are incorporated, and also because the signal component from blood is contaminated by cerebrospinal fluid/free water.

One study was dedicated to exploring the IVIM parameters at different field strengths and the influence of relaxation and signal-to-noise ratio (SNR) was observed. Although the repeatability was generally better at higher magnetic field strength, it was shown that the relaxation properties and an unexpectedly low SNR at high field strengths resulted in erroneous blood volume estimates. The model commonly used for IVIM data analysis was then modified to compensate for relaxation effects, based on literature values. When this correction was performed, results from the lower field strengths showed lower discrepancy from expected values, while the results from higher field strength were still erroneous, likely due to physiological noise.

In a following project, relaxation times were actually measured during the data collection, and incorporated to compensate for relaxation and improve the fitting procedure. The model was also upgraded to a three-compartment model to better describe the underlying tissue by including the cerebrospinal fluid component. Compared to a non-relaxation-compensated model, the three-compartment model with relaxation-compensated data modified the obtained results and reduced the CSF contamination.

The last IVIM project also included a three-compartment model, but in this case the purpose of the third compartment was to improve the quantification of the fraction of free water. The free water fraction has been established as a source of clinically useful image contrast, pointing at pathologies that affect the extracellular space, for example, atrophy and neuroinflammation. With our model, the bias from microcirculation was reduced in the free water estimate. A model where extracellular and microvascular effects can be separated might enable new diagnostic possibilities.

Populärvetenskaplig sammanfattning

Blodet bär med sig syre och näringsämnen som är vitala för vävnadens överlevnad, och därför är karakterisering av hjärnans blodförsörjning av stor betydelse. Blodflödet i kapillärerna kallas för perfusion. Vid MRI-baserad perfusionsmätning i hjärnan utnyttjas ofta signalförändringar orsakade av ett spårämne i blodet. Spårämnet kan antingen skapas internt genom märkning av det arteriella inflödet av blod eller tillföras utifrån via intravenös injektion av ett kontrastmedel. Mätning av signalförändringar när blod med kontrastmedel passerar vävnaden brukar benämnas dynamisk kontrastförstärkt bildtagning. Kontrastmedelsanvändning kan dock vara problematisk under vissa förhållanden, och forskning tyder på att konventionella MR-kontrastmedel kan stanna kvar länge i vissa vävnader. Det aktuella avhandlingsarbetet fokuserar därför främst på utveckling och utvärdering av helt icke-invasiva metoder för bedömning av mikrocirkulation, samt även i viss mån kvantifiering av mikrostrukturer.

MRI-baserade diffusionsmätningar bygger på mätning av den signalattenuering som sker när vattenmolekyler rör sig slumpmässigt i vävnaden, i närvaro av en magnetfältsgradient, och metoden används framför allt för karakterisering av nervbanornas integritet samt vävnadens mikrostruktur. Vi har använt en diffusionsteknik, s.k. *q*-space-analys, för att mäta storleken på fibrer i ett biologiskt fantom med en klinisk MR-kamera, som ett steg mot att förstå metoden bättre i denna miljö, då metoden tidigare framför allt använts i NMR-spektrometrar där hårdvaran har högre prestanda.

Med s.k. "intravoxel incoherent motion (IVIM) imaging" mäter man effekter av både diffusion och perfusion i vävnaden, och man kan också separera dessa effekter. Detta är en skonsam och icke-invasiv metod som varken utnyttjar joniserande strålning eller kontrastmedel. I våra studier har IVIM-metoden utvärderats på MR-kameror med olika fältstyrkor, och modellen som används för att beräkna perfusionsrelaterade parametrar har utvecklats för att kunna anpassas till hjärnans olika vävnadstyper och vattenpopulationer på ett mer komplett sätt. I våra studier har vi dragit slutsatsen att IVIM är en teknik som kräver mycket optimering, både vid val av MR-maskinvara, bildtagningsparametrar, bildbehandling, modell och analysmetod. Trots detta kan metoden användas på olika sätt, och ge intressanta resultat.

List of original papers

I. Jimmy Lätt, Markus Nilsson, **Anna Rydhög**, Ronnie Wirestam, Freddy Ståhlberg, Sara Brockstedt. Effects of restricted diffusion in a biological phantom: a q-space diffusion MRI study of asparagus at a 3T clinical scanner. *Magnetic Resonance Materials in Physics, Biology and Medicine. 2007; 20(4):213-222*.

II. **Anna Rydhög**, Matthias J. P. van Osch, Emelie Lindgren, Markus Nilsson, Jimmy Lätt, Freddy Ståhlberg, Ronnie Wirestam, Linda Knutsson. Intravoxel incoherent motion (IVIM) imaging at different magnetic field strengths: What is feasible? *Magnetic Resonance Imaging. 2014; 32(10):1247-1258*.

III. **Anna S. Rydhög**, Ofer Pasternak, Freddy Ståhlberg, Ronnie Wirestam, Linda Knutsson, André Ahlgren. Estimation of diffusion, perfusion and fractional volumes using a multi-compartment relaxation-compensated signal model. *Manuscript*.

IV. **Anna S. Rydhög**, Filip Szczepankiewicz, Ronnie Wirestam, André Ahlgren, Carl-Fredrik Westin, Linda Knutsson, Ofer Pasternak. Separating blood and water: Perfusion and free water elimination from diffusion MRI in the human brain. *NeuroImage. 2017; 156:423-434.*

List of contributions

Here is a summary of my contributions to each original paper included in this thesis:

I. I was responsible for the choice of a suitable phantom for the purpose of the study. I participated in the design of the study and participated in all MRI data acquisitions as well as in the microscopy measurements. I contributed to the data analysis and to the writing of the paper.

II. I contributed significantly to the study design. I carried out all of the data acquisition, part of the post-processing and performed all of the analysis. I was the main author of the paper.

III. I contributed significantly to the study design and I participated in the changes made to the available pulse sequence code. I participated in all data acquisition and I performed the data analysis. I was the main author of the manuscript.

IV. I made major contributions to the study design and carried out the data acquisition on the healthy volunteer. I did most of the post-processing, and I performed all the data analysis. I was the main author of the paper.

Abbreviations

AD	Axial Diffusivity
ADC	Apparent Diffusion Coefficient
AIF	Arterial Input Function
ASL	Arterial Spin Labelling
COM	Centre Of Mass
CBF	Cerebral Blood Flow
CBV	Cerebral Blood Volume
CSF	Cerebrospinal Fluid
D	Diffusion coefficient
DCE	Dynamic Contrast-Enhanced
DSC	Dynamic Susceptibility Contrast
DTI	Diffusion Tensor Imaging
DWI	Diffusion Weighted Imaging
FWHM	Full Width at Half Maximum
FWTM	Full Width at Tenth Maximum
IVIM	Intravoxel Incoherent Motion
dMRI	Diffusion Magnetic Resonance Imaging
MRI	Magnetic Resonance Imaging
MTT	Mean Transit Time
NMR	Nuclear Magnetic Resonance
SNR	Signal-to-Noise Ratio
OGSE	Oscillating Gradient Spin-Echo
PD	Proton Density
PGSE	Pulsed Gradient Spin Echo
RD	Radial Diffusivity
SAR	Specific Absorption Rate
STEAM	STimulated Echo Acquisition Mode
SGP	Short Gradient Pulse
T1	Longitudinal Relaxation Time
T2	Transverse Relaxation Time
T_D	Diffusion Time
TE	Echo Time
TR	Repetition Time

1. Introduction

Brain research has progressed considerably in the last decades, partly due to the introduction and development of new imaging techniques that allow in vivo visualization and quantification of brain architecture and function. The research described in this thesis focuses on two such methods, i.e. perfusion MRI and diffusion MRI (dMRI).

Perfusion MRI aims to provide insights into the transport of blood in the microvasculature. Blood carries oxygen and nutrients vital for tissue survival, and characterization of the brain's supply of blood is thus crucial. In a typical perfusion measurement, observed dynamic signal changes caused by contrast enhancement in the blood are analysed. The administered contrast agent may, however, be problematic in certain circumstances, especially for patients with insufficient renal function because they have an increased risk of developing nephrogenic systemic fibrosis (1), a debilitating disease. It has also quite recently been shown that gadolinium-based contrast agents, normally used in MRI, are deposited and retained in tissue (2-6). Also in paediatrics, and in cases where subsequent measurements are needed, a non-invasive method without the use of contrast agents is of significant clinical value.

Diffusion MRI is an imaging technique sensitive to the thermal micro-displacement of water molecules. It is the time scale of the experiment that dictates the length scale of the observed water diffusion, and typically this time, the diffusion time (T_D), is about 40-60 ms. This implies that without flow water molecules can move up to approximate distance of 10-20 μm during the experiment, according to Einstein's diffusion equation (7). Since this distance is in the order of cellular structure sizes (8), it has been suggested that dMRI measures are affected by these structures and can therefore be used to study them. If T_D is shortened, the interaction between the water molecule and the surrounding structures is reduced. Changing T_D is thus a tool for gaining insight into the barriers present in the neuronal tissue and the separation between them.

The pseudo-random movement of blood in the capillary system may practically appear like random motion pattern of diffusing water and is therefore also picked up in the measured signal from a diffusion experiment. In MRI, the image elements represent voxels, i.e. 3D volume elements containing the measurable information in each position. Hence, the signal originating from a voxel where both blood perfusion and extravascular water diffusion exist contains information about both these

compartments. The method in which information from each of these compartments is separately quantified is commonly referred to as intravoxel incoherent motion (IVIM) imaging (9). This is an appealing concept, especially due to its non-invasiveness in quantifying perfusion-related parameters and the ability to provide combined information about diffusion and perfusion, which is of potential usefulness, for example, in ischemic stroke assessment (10-13). IVIM imaging is a method that has been subject to some debate, but it has nevertheless regained increasing interest during recent years, due to, for example, a general increase in image signal-to-noise ratio (SNR) and improved tools for data analysis.

In reality, a voxel contains more than two compartments, and free water is one that may contribute significantly to the IVIM signal. Free water is defined as water molecules that do not experience coherent flow and are not restricted or hindered by their surroundings during a typical diffusion time (14). In many cases, the free water is a confounding factor, which generates a signal component that should be eliminated since it contaminates the diffusion result representing tissue or blood. This free water contamination can be removed by incorporating it in the model describing the diffusion signal (15). However, it should also be noted that the free water is a parameter that can be used in the diagnosis of diseases linked to, for example, inflammation and atrophy (16-21).

1.1 Aims

The primary aims of the studies reported in this thesis were:

Paper I: To find a suitable biological phantom for studying the effects of varying T_D on restricted diffusion with a clinical scanner, using a q-space imaging technique in which the full width at half maximum (FWHM) of the displacement distribution was measured.

Paper II: To study how the IVIM method performs at different magnetic field strengths (1.5, 3 and 7 T), with focus on quantification of cerebral blood volume (CBV) and how SNR and relaxation properties affect the results at the different field strengths.

Paper III: To study the value of an extended IVIM model, i.e. a three-compartment model where signal components from diffusion, perfusion and CSF are included and where relaxation effects are incorporated to better distinguish between these compartments.

Paper IV: To study the effect of the blood component on the estimation of free water, and to remove this bias by separating the three different signal components arising from tissue, blood and free water. The study was performed using simulated and experimental data from a typical diffusion experiment and from an acquisition with a more comprehensive gradient scheme.

2. Diffusion MRI

When molecules are in a state where the chemical potential gradient is zero, they still move due to random thermal collisions with neighbouring molecules. The phenomenon is called self-diffusion or Brownian motion, and the net displacement caused by this motion depends on the inherent energy (dependent on temperature) and on the viscosity of the medium (22). Einstein connected Brownian motion to Fick's laws of diffusion (7), which explain the movement of particles from a region of high concentration to a region of low concentration, by explaining how the displacement of molecules can be quantified by the diffusion coefficient (D). As it turns out, these small displacements described by D (in units of length squared per unit time) can be quantified using motion-induced alterations in the detected MR signal.

The static magnetic field is never truly homogeneous, due to, for example, imperfections of the magnet, or due to local variations of magnetic susceptibility in the imaged object, warping the magnetic field lines. As a result, the Larmor frequency varies slightly across locations, yielding more rapid transverse relaxation than what is expected from the inherent T2 of the object. The spin echo sequence was introduced by Hahn in order to compensate for static magnetic field inhomogeneities (23). Hahn added a 180° RF pulse to a basic MR experiment, thereby cancelling the dephasing that was caused by static field inhomogeneities. Hahn also predicted that some of the dephasing would not be compensated, i.e. signal attenuation due to random processes such as spin-spin interactions (T2 relaxation) and small-scale random spin motion in the magnetic field gradient. By isolating this random spin motion, the self-diffusion process itself can be measured (24). Many years later, diffusion imaging has become an important diagnostic tool, especially following the discovery that diffusion-weighted images could depict ischaemic stroke lesions already within the first minutes of infarction onset (25), which T2-weighted images were unable to show (26).

2.1 Diffusion Encoding Using MRI

Stejskal and Tanner were the first to estimate the diffusion coefficient from an NMR experiment (27, 28), and they used a pulsed gradient spin echo (PGSE) sequence (Figure 1a) that activates a magnetic field gradient during a spin echo experiment,

creating a known magnetic field inhomogeneity. With this modified T2-weighted sequence, molecular displacement can be detected by using one 90° RF pulse followed by two balanced gradient pulses separated by a 180° RF refocusing pulse. The first gradient pulse introduces a phase shift to encode the spatial starting positions of the spins. After a diffusion time, T_D, the second gradient is applied which refocuses the phase evolution. Spin displacements occurring during the diffusion time will not be fully refocused, and the incoherent motion pattern of the spin population results in a phase dispersion remaining at the echo time (TE). This causes an additional signal attenuation directly linked to the net molecular displacement during T_D. For a Gaussian distributed displacement, this signal attenuation will be dependent on the diffusion coefficient, D, of the water molecules, as

$$S/S_0 = e^{(-(\gamma g \delta)^2(\Delta-\delta/3)D)} = e^{-bD} \quad (2.1)$$

where S is the diffusion-weighted signal amplitude, S_0 is the non-diffusion-weighed signal, γ is the gyromagnetic constant, g is the amplitude of the applied gradient, activated for the duration δ, and Δ is the separation in time between the starting points of the two gradients.

To measure the diffusion coefficient, one would normally run a series of experiments where either the duration or the amplitude of the gradients is incremented from one experiment to another. The expression (Δ-δ/3) is the effective diffusion time T_D, and, as mentioned above, this is the time period during which the spin movements are measured. The product $(\gamma\ g\ \delta)^2$ (Δ-δ/3) is known as the b-value. In PGSE experiments, this b-value, together with the direction of the diffusion encoding, are the tuneable parameters. Equation 2.1 shows that the measured signal attenuation is more pronounced when large b values are used and when diffusion is high.

Interestingly, the mean square displacement can be calculated from D, using Einstein's expression for the mean squared molecular displacement, $\langle x^2 \rangle$:

$$< x^2 >= 2DT_D \quad (2.2)$$

The root of $\langle x^2 \rangle$ then represents the average molecular displacement and, as can be seen from Equation 2.2, it increases linearly with the square root of T_D. This equation only works for free diffusion, i.e. diffusion displacements following a Gaussian distribution. Using this relationship it is found that 68 % of water molecules, moving without encountering any boundaries, have been displaced within a distance of 17 µm in 50 ms, if body temperature is assumed (29).

Another pulse sequence used for diffusion MRI is the stimulated echo acquisition mode (STEAM) sequence, in which the 180° pulse used in PGSE is replaced by two 90° pulses (Figure 1b). In the PGSE sequence, the signal decays with T2 during the echo time, while in the STEAM sequence the signal decays at the rate of T1 during

the so called mixing time (TM), i.e. the time which determines the diffusion time in a STEAM sequence. This mixing time is defined as the time between the two STEAM-specific 90° pulses. The STEAM sequence stores the magnetization along the longitudinal axis, thus reducing the effective T2 relaxation which allows for longer diffusion times to be used. Hence, this sequence is particularly advantageous in comparison with the PGSE when diffusion times are long in comparison with T2, and T1>>T2.

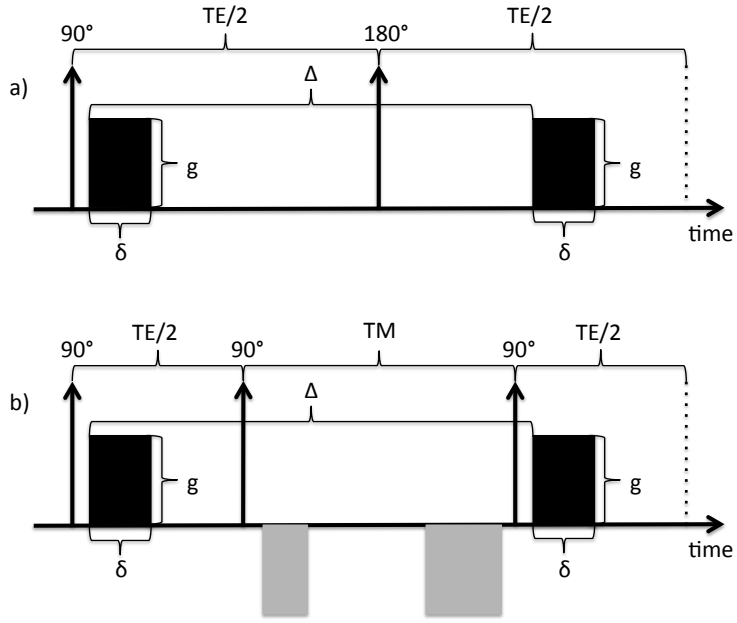

Figure 1. a) The pulsed gradient spin echo (PGSE) pulse sequence. b) The stimulated echo acquisition mode (STEAM) squence utilizing three 90° RF pulses, used in the experiments for Paper I. The black blocks symbolize the diffusion-encoding gradients, and the grey blocks symbolize the gradients used for eddy current compensation and spoiling of unwanted signal contributions from the second RF pulse. Gradient duration (δ), amplitude (g) and duration (Δ) are marked out, as well as the mixing time (TM) and the TE/2 times. The dashed line indicates the time in which the signal echo is detected.

Although long diffusion times can be obtained with the STEAM sequence, a disadvantage is that half of the signal is lost when the net magnetization is placed along the longitudinal axis. Another disadvantage of the STEAM sequence is that additional gradients, such as slice-selective or crusher gradients placed around the 90° RF pulses, may contribute to the diffusion weighting and therefore introduce a shift in the diffusion-encoding direction (30). However, this can be compensated for by adjusting the directional scheme (31).

In q-space imaging the signal attenuation is expressed in terms of the wave vector $\boldsymbol{q}$ instead of b, where $\boldsymbol{q} = (2\pi)^{-1}\gamma\delta\boldsymbol{g}$. The signal decay of a diffusion weighted image (DWI), S($\boldsymbol{q}$), can be modelled as (32):

$$S(\boldsymbol{q}) = \int P(\boldsymbol{r}|\Delta)e^{i2\pi\boldsymbol{q}\boldsymbol{r}}d\boldsymbol{r} \quad (2.3)$$

P is the probability density function (PDF) for a molecule to show a displacement $\boldsymbol{r}$ following the diffusion time Δ and assuming a homogeneous water molecule concentration across the voxel. In the dMRI experiment, each water molecule acts as a probe of its immediate surroundings since its displacement is affected by the microstructural geometry of the medium. The DWI signal is the weighted sum of the effects of all displacements and reflects the mean displacement in the entire voxel. The PDF, P, however, reflects all of the various displacements. It is therefore the shape of P that connects the measurement signal, molecule displacements and the entire geometry, i.e. parameterizing or explicitly extracting P is an important task in the analysis of diffusion images.

2.2 Restricted and Hindered Diffusion

The effect of the molecular movement on the resulting MR signal depends on the underlying structure of the studied material. Water molecules are present at a relatively constant concentration in all types of brain tissue. Yet the architectural differences between each region imply that the water molecules are hindered by different geometrical constraints, and this affects the signal obtained from dMRI. These obstacles might be fibres, cell membranes or macromolecules, and there may also be locations where the water molecules are confined by electrical charges in proteins or in the surface of the cell membrane. When water molecules are restricted or hindered by such obstacles, the diffusion can no longer be described by the Gaussian distribution according to Einstein's equation.

Because of these inhomogeneities in biological materials, such as in tissue, diffusion is often characterized by what is known as the apparent diffusion coefficient (ADC). The ADC was originally introduced to account for all types of incoherent motions, including microvascular perfusion in the capillary bed (33), and is thus a parameter that is generally intended for homogenous tissue where it is likely to constitute a fair estimate of the mean diffusion.

The effects of non-Gaussian displacements on the measured signal, and how they should be modelled, are not yet fully understood (34), but restriction can be defined by the dimensionless variable ζ as

$$\zeta = DT_D/R^2, \quad (2.4)$$

assuming that the particles under investigation are confined to a sphere of radius R (35). In a medium where there are reflecting boundaries, the diffusion time, T_D, thus becomes very important, and one way to study restriction is by looking at differences in the obtained signal when T_D is changed. For a small T_D or a large R, the studied molecules will appear free. As T_D increases, or R decreases, ζ approaches one, and in cases where the molecules have bounced several times, they will appear restricted.

The centre of mass (COM) of the distance travelled by a water molecule depends on how many times it has bounced against the barriers. The molecules will not have time to move when T_D is infinitesimally short ($\zeta << 1$), but as T_D increases, the COM will move towards the centre of the confinement (36). To perform accurate q-space imaging of restricted diffusion, T_D must be long enough to allow the molecules to diffuse across the whole constrained volume. This is often referred to as the long diffusion time limit.

Water molecules in biological materials are thus often considered to be hindered instead of restricted, which means that the particles appear as if they resided in a more viscous substance. The reason may be cell membranes, axon fibres, or other obstacles, which constrain the water molecule movement and preclude truly free diffusion.

2.2.1 Using q-space for Measurements of Restricted Diffusion

The q-space MR imaging concept has the advantage of providing information about the microstructure without invoking assumed models of the system. Instead, quantification of the diffusion displacement is accomplished through the Fourier relation between P and the signal decay measured with multiple gradient strengths (Equation 2.3). The q-space approach was developed to measure structure sizes (37) and originally used for studies of porous material in NMR scanners (32, 38, 39). The q-space imaging concept was later introduced in a clinical setting (40) and has been shown to provide metrics of suggested value in studies of dementia (41), Parkinson's disease, multiple sclerosis (42) and autism (43). Axonal diameter is here an interesting target, since it is proposed to be related to the conduction speed of action potentials between the neurons (44, 45).

In the study reported in Paper I, we brought this type of measurement to a clinical scanner, by utilizing a biological phantom for structural q-space studies. We used asparagus (*Asparagus officinalis*), which has a structure consisting of aligned vascular capillaries in the stem, known to generate anisotropic diffusion (46). The purpose of the study was to investigate the possibility of absolute quantification of the fibre dimensions in this phantom, using the full width at half maximum (FWHM) of the diffusion propagator.

The FWHM of the diffusion propagator is one of the parameters that can be obtained from the q-space analysis and it is related to the average displacement of the diffusing molecules. FWHM is thus a parameter used for determining structural sizes

much smaller than what can be resolved by conventional MR imaging. Other ways to quantify aspects of the displacement distribution are through the height of the distribution, the probability of zero displacement, *P(0)*, or the full width at tenth maximum (FWTM). Structural sizes have previously also been estimated from *q*-space dMRI using the initial slope approach (47) and the diffractogram method (48). Both of these methods suffer from problems when the studied system consists of a distribution of compartment sizes and when the system is complex, for example, when membranes or compartment surfaces are not parallel (47, 49). Hence, these types of measurements are not readily feasible in clinical practice.

The sizes of the asparagus capillaries, measured with microscopy (Zeiss WL research microscope), are distributed between 4 and 50 μm, with a mean diameter of 20 μm. This value is similar to the larger diameter sizes of white matter axons in the human brain, which typically are between 0.2 and 20 μm (8). The FWHM measured perpendicular to the asparagus capillaries increased as T_D was protracted. At a T_D of approximately 100 ms, the FWHM converged to a constant value when the long diffusion time limit was approached. Parallel to the capillaries, a linear increase of the FWHM was observed, although not at the same rate as for free water. Diffusion in this direction could thus be considered as hindered.

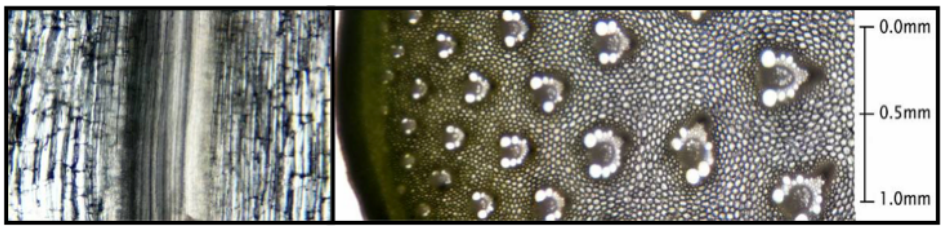

Figure 2. To the left is a microscopy image of the asparagus along the fibres, and to the right is a microscopy image across the fibre structure. Measurements in the microscopy images indicated that the vascular bundles of the capillaries consisted of diameters between approximately 4 μm and 50 μm, with a mean diameter of 20 μm.

The gradient pulse length δ is important to consider in displacement measurements with the *q*-space method. If δ is too long, the movement of the water molecules during the pulse cannot be neglected, which results in errors when using Equation 2.3, and the measured FWHM will no longer be correct. To avoid this, the short gradient pulse (SGP) approximation must be fulfilled. The SGP approximation requires that $\delta >> a^2/D$, where a is the size of the confinement (50). This condition is possible to fulfil in the NMR environment, where the gradient amplitudes are high, whereas it has to be violated in clinical MRI scanners in order to reach high enough *q*-values, i.e. providing sufficient resolution to resolve axonal sizes.

In our study (Paper I), the SGP condition was examined by increasing δ from 24 to 74 ms, which led to the observation of a statistically significant reduction in

FWHM from 19 to 16 μm. The study provided evidence of restricted diffusion in the asparagus, with a constant FWHM observed as T_D increased, and a reduced FWHM as δ increased. It also showed that this type of size estimation was possible with a clinical MRI scanner. However, when the SGP condition is violated, estimated compartment sizes will be underestimated. To overcome this problem it may be possible to use a mathematical framework which has been developed to enable accurate estimates of compartment dimensions even when the SGP is not fulfilled (51).

The *q*-space method has, at this point, not become a widespread clinical tool for measurement of axon diameters. Among the reasons are difficulties reaching sufficiently high resolution with clinical MRI units (52), e.g. sufficiently strong gradient strengths and high slew rates (53). Also, the SNR penalty associated with high *q*-values limits the image resolution with this technique (54). Furthermore, it is a method which requires long scan times (54). Methods such as AxCaliber (55) and ActiveAx (56) have gained more interest during recent years. AxCaliber is a method to measure mean axon diameters using one fixed gradient direction and multiple diffusion times and gradient strengths in a PGSE sequence. The model has components describing restricted diffusion, hindered diffusion, and free diffusion, and each compartment has its own diffusion coefficient, size, volume fraction, membrane permeability, and relaxation times. ActiveAx is an extended and optimized version of the methods used in AxCaliber. With ActiveAx one can determine the accuracy and precision of the axon diameter estimation. Also, the use of oscillating gradient spin-echo (OGSE) sequences in diffusion spectroscopy allows for very short diffusion times to distinguish small diameter sizes without the need for extreme gradient strength. OGSE together with the PGSE methods is also a promising tool to study a variety of axon sizes (57-59).

2.3 Isotropic and Anisotropic Diffusion

The consequence of the MR diffusion-encoding process is that diffusion is only measured along the direction of the applied field gradient, even though diffusion is a three-dimensional process. The operator can control the diffusion encoding by varying the direction and amplitude of the field gradient applied. In biological materials, the diffusion constant describing the movement of the water molecules usually varies with the direction, due to directionally varying hindrances and restrictions. This causes a microscopically heterogeneous environment in which the diffusion is directionally dependent, i.e. the diffusion is anisotropic. Anisotropy in biological materials was observed as early as in the 1970s (60, 61), but this feature was not studied *in vivo* until in the late 1980s (26, 62). In white matter, the anisotropy arises mainly from the organization of myelinated axonal fibres in bundles, where the

diffusion along the fibres is higher than in the perpendicular direction. In the study described in Paper I, an asparagus phantom, where water moved predominantly along the fibres rather than perpendicular to them, was employed to characterize fibre diameters using q-space diffusion MRI.

When the motion is independent of the direction, the diffusion is said to be isotropic. The isotropy either arises from isotropically restricted diffusion, or from free diffusion when no obstacles affect the movement of the water molecule. Nearly isotropic diffusion can be found in cerebrospinal fluid (CSF) and in oedema (63).

2.4 Tensor Representation of Diffusion

The most common method for deducing the geometry of the tissue from water displacement is diffusion tensor imaging (DTI). In DTI, which models displacements in multiple directions using a diffusion tensor (64), the diffusion is described by a 3×3 symmetric matrix (tensor) of diffusion coefficients, instead of a single coefficient. The geometry of the underlying tissue structure is inferred from the DTI indices, which are tensor invariants based on the spectral decomposition of the tensor (65).

The Gaussian diffusion model used by Stejskal and Tanner was generalized by Basser et al. (64), to a model where the PDF is regulated by a three-dimensional diffusion process. Instead of the relation presented in Equation 2.1, the solution to this tensor representation of the diffusion becomes:

$$S(q_k)/S(0) = e^{-b\boldsymbol{q}_k^T \boldsymbol{D} \boldsymbol{q}_k} \tag{2.4}$$

where $\boldsymbol{q}_k$ is the k:th applied diffusion gradient direction. The diffusion tensor has a spectral decomposition described as

$$D = \sum_{a=1}^{3} \lambda_a \boldsymbol{U}_a (\boldsymbol{U}_a)^T \tag{2.5}$$

for three eigenvectors $\boldsymbol{U}_a$ and three positive eigenvalues λ_a. This spectral decomposition provides a diffusion ellipsoid representation with the radii oriented along the eigenvectors, and with the respective lengths described by the corresponding eigenvalues (64, 66). Diffusivity along the principal direction, λ_1, is often called axial diffusivity (AD) and the diffusivities along the shorter axes are usually averaged, $(\lambda_2 + \lambda_3)/2$, to generate the radial diffusivity (RD). The advantage of using the diffusion tensor model instead of the average diffusion coefficient is that it can account for anisotropic diffusion, where the ADC depends on the measurement direction. In addition, the tensor's geometric representation can more easily be related to tissue structures. In Paper IV, a tensor model was used to describe the tissue diffusion in the three-compartment IVIM model describing tissue, blood and free water.

Differences in the geometries of white and grey matter correspond to different shapes inferred by the tensor's spectral decomposition. It was experimentally shown that diffusion in voxels containing homogeneous white matter is best fitted with cigar-shaped ellipsoids ($\lambda_1 \gg \lambda_2 \simeq \lambda_3$) (67), which imply the tubular shape of the axons. Other normal intracranial compartments, i.e. grey matter and CSF, are best fitted with isotropic, sphere-shaped tensors (67).

The mean diffusivity (MD) is a feature that can provide a meaningful contrast mechanism for identifying changes in bulk diffusivity, such as an increase in tissue water content. It is calculated as

$$\mathrm{MD} = \mathrm{mean}(\lambda) = \mathrm{Trace}\,(D)/3, \tag{2.6}$$

where the trace equals (D_{xx}+D_{yy}+D_{zz}) (68).

Another unique feature of the tensor model is the fractional anisotropy (FA) (67). It is the normalized variance of the eigenvalues, i.e.

$$\mathrm{FA} = \sqrt{\frac{3((\lambda_1 - MD)^2 + (\lambda_2 - MD)^2 + (\lambda_3 - MD)^2)}{2(\lambda_1^2 + \lambda_2^2 + \lambda_3^2)}} \tag{2.7}$$

FA can take values between 0 and 1, where in GM and CSF the FA is low, and in WM it is high.

In Paper I, we reported the use of FWHM-based tensors, i.e., we used FWHM instead of D to construct tensors describing the anisotropy in the asparagus phantom. This FWHM tensor analysis yielded more accurate results compared to direct measurements in the three orthogonal directions.

2.5 Free Water and the Two-Compartment Diffusion Signal Model

Free water is defined as water molecules that are not restricted or hindered by their surroundings and do not experience coherent flow. In the human brain, free water is found as CSF confined to the ventricles and around the brain parenchyma. It may also accumulate in the form of vasogenic oedema within the brain parenchyma in the extracellular space, caused by processes such as tumours, cerebral abscesses, brain trauma, or haemorrhage that cause ruptures in the blood brain barrier (26, 69, 70). Free water can be identified by DTI since it shows isotropic diffusion with an ADC of about 3×10^{-3} mm^2/s at 37°C, approximately 3-4 times higher than the typical ADC values of the brain parenchyma (65).

Free water has been known to cause partial volume contamination in voxels shared by CSF and brain tissue, i.e. on the outlines of the ventricles and close to the peripheral borders of the brain parenchyma (14, 16, 71, 72). As a result, CSF-contaminated voxels typically show increased ADC estimates. A white matter voxel contaminated by free water will most likely be fitted with a relatively isotropic diffusion tensor, which disqualifies it from being interpreted as white matter. CSF contamination has been shown to affect the delineation of fibres that pass near the ventricles, such as the fornix, the cingulum, and parts of the corpus callosum (72-74), and to be a limitation in voxel-based and histogram analysis comparisons of DTI-related quantities (75). Oedema has a similar effect as CSF contamination, although its location and spread depend on the localization of the pathology that caused it. In addition, oedema usually infiltrates brain tissue, contaminating large areas with partial volume effects that make the infiltrated tissue challenging to identify and tractography analysis unfeasible (76, 77).

One proposed method for eliminating CSF contamination is to use a fluid-attenuated inversion recovery diffusion weighted imaging (FLAIR-DWI) sequence, which suppresses the CSF signal (72-74). However, FLAIR-DWI has several drawbacks: it usually does not correct for oedema contamination (due to different T1-relaxation times of CSF and oedema), it suffers from low SNR, it increases the scan time, it increases the specific absorption rate (SAR), and it does not allow cardiac gating required to prevent artefacts due to pulsation and misalignment (74, 78). Instead, a model-based approach has been introduced for eliminating CSF contamination from conventional diffusion images (15), using a bi-tensor model that has two compartments, i.e. one free water compartment, with the fractional volume, f_w, characterized by isotropic tensor with diffusivity of free water, D_w, and one tissue compartment, with the fractional volume (1-f_w), modelled by a diffusion tensor $\boldsymbol{D_t}$ as

$$S_i = S_0 \left[f_w \cdot e^{-b_i D_w} + (1 - f_w) \cdot e^{-b_i \boldsymbol{g}_i^T \boldsymbol{D_t} \boldsymbol{g}_i} \right], \tag{2.8}$$

where no exchange between the compartments is presumed (14, 79, 80). From $\boldsymbol{D_t}$ and its eigenvalues, free-water-corrected values of RD and AD as well as the FA can be calculated. Since vasogenic oedema has diffusion properties similar to free water and causes similar partial volume effects as CSF contamination, it was suggested that minimizing CSF contamination in this way might also reduce the effect of oedema on the signal attenuation.

The bi-tensor model introduced fitting problems, which has been solved by increasing the number of measurements and *b*-values, at the cost of increased scan time (15). Pasternak et al. used an alternative approach for the free water elimination instead, by applying a regularization framework and simultaneously obtaining a voxel-wise map of the amount of free water which was shown to have clinical value (14, 81). Compartmental models are also used to eliminate CSF contamination in other

diffusion methods such as NODDI (82), AxCaliber (83) and diffusion basis spectrum imaging (84).

The free water signal fraction (f_w), obtained from these models, is the relative signal contribution of free water in each voxel. Interestingly, it has been shown that contrast based on free water provides meaningful clinical information, because it allows monitoring of extracellular changes, associated with neuroinflammation and/or atrophy in, for example, normal aging (16), traumatic brain injuries (21), schizophrenia (17, 18), Parkinson's disease (20), mild cognitive impairment and Alzheimer's disease (19, 85, 86).

The bi-tensor model for diffusion is a good approximation in many brain regions, because it is able to correct for most extracellular water effects on estimated DTI parameters (17, 87). However, it has also been shown that f_w is overestimated in some areas, for example, the fornix (17, 19, 20), and one reason for this might be the contribution from perfusion, which is another fast component that causes attenuation of the measured signal. Even though only a small fraction of blood perfusion is expected in brain tissue (a few percents), our simulations have shown that it may cause a significant overestimation of the f_w parameter (Paper IV), as seen in Figure 3.

In both Paper III and Paper IV, we explore approaches to the finding that both free water/CSF and perfusion, in addition to the tissue diffusion, can cause signal attenuation in a diffusion experiment.

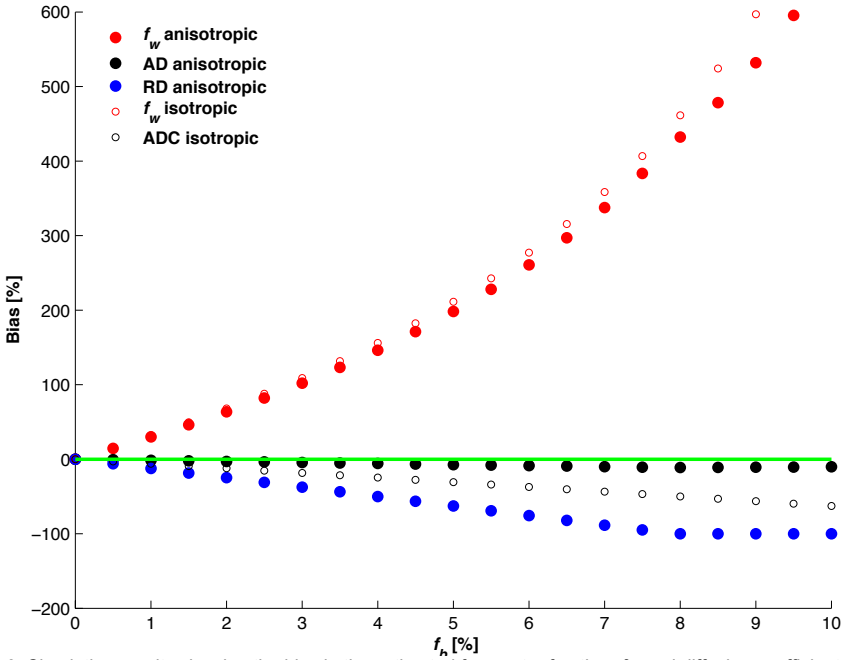

Figure 3. Simulation results showing the bias in the estimated free water fraction, f_w, and diffusion coefficients (AD and RD) when the blood fraction, f_b, was changed from 0 to 10% (from Fig 1a in Paper IV). This figure illustrates the large effect of capillary blood flow on the f_w estimation, even though the contribution from blood is very small.

One common method to overcome this contribution from the blood pool is to remove data known to be affected by this component, i.e. the low *b*-value data (88). However, the *b*=0 acquisition is often included in the analysis because it increases the contrast between high and low b-value signals, and the problem with this approach is that the signal at *b*=0 is influenced by all water pools, including the perfusion effect.

3. Perfusion MRI and IVIM

Perfusion imaging using MRI includes methods used for evaluation of tissue properties related to the microcirculation and the microvasculature. The tissue perfusion is crucial to ensure a sufficient supply of nutrients to the constituent cells, removal of metabolic by-products and maintenance of a constant tissue temperature. The calculated parameters are often visualized in terms of relative regional differences, but perfusion MRI can also be used to retrieve quantitative absolute measures. Since the vasculature adjusts the perfusion in order to meet the metabolic demand of the tissue, perfusion imaging can provide indirect measures of tissue metabolic activity (89).

Methods using gadolinium complexes as exogenous tracers are generally robust, and constitute the most widely used clinical MRI techniques for perfusion assessment. In these methods, the presence of the contrast medium causes a relaxation-induced change in signal intensity during dynamic imaging. Dynamic contrast-enhanced (DCE) MRI (90) and dynamic susceptibility contrast (DSC) MRI (91) are gadolinium-based methods which can produce estimates of perfusion, perfusion-related parameters and transcapillary permeability, but with the disadvantage of requiring a correct estimate of the arterial input function (AIF), which is often difficult to extract.

Endogenous tracer methods use the blood water itself as a tracer. Arterial spin labelling (ASL) is one such method where the longitudinal magnetization of blood water in a tissue-feeding artery is inverted or saturated (referred to as labelling), and the signal intensity is then reduced when the target tissue of interest is subsequently imaged (92, 93). The signal change caused by the inflowing labelled blood is very small, and therefore an image subtraction between data with and without labelling, often in combination with signal averaging, is needed to enhance the contrast-to-noise ratio. This subtraction also effectively removes the signal from static tissue, yielding a relative perfusion image.

Ideally, the absolute blood flow per unit of tissue mass should be estimated for each voxel (in millilitres of blood per minute per 100 grams of tissue). That would allow for identification of small perturbations of the blood flow in absolute terms, as well as relating the perfusion to vital threshold levels. But absolute quantification is difficult to achieve with both exogenous and endogenous tracers since many factors have to be taken into account for correct modelling of the signal. Although there are perfusion parameters that have been proposed for descriptive-only characterization of the

contrast-agent-induced signal change, such as area under the curve and time to peak signal enhancement, they depend on arterial input, capillary transit times, sequence type and calibration methods and they also tend to vary between study centres (94). The advantage of MR perfusion techniques are their low degree of invasiveness with no need for exposure from ionizing radiation, and their ability to yield estimation of tissue perfusion relatively quickly with good spatial resolution and in immediate connection with high-quality morphological imaging (95).

IVIM imaging is an alternative method for estimation of microvascular parameters without the need for contrast agent injection (9, 96). IVIM contrast is based only on motion encoding and read-out in the same volume, and is therefore independent of the path the blood has taken to reach the region of interest. This can be advantageous in cases where blood flow is slow, for example, in stroke or severe carotid artery stenosis, where blood supply is conserved by collaterals. Also, since the IVIM method is based on a completely different methodology than the other perfusion methods, it might provide supplementary information.

3.1 Cerebral Haemodynamics and Microvasculature

Perfusion is a term describing the passage of blood through the microvascular network and the supply of blood to an element of tissue. The vascular compartment contains the blood that mainly consists of plasma, red blood cells, white blood cells and platelets. The extravascular compartment consists of tissue cells and extracellular space. Blood delivers oxygen, nutrients and other circulatory agents to the tissue, and removes carbon dioxide and other waste products from it. Blood flows in the vascular tree from the large arteries into smaller and smaller vessels, finally to the arterioles and into the capillaries. Oxygen, nutrients and other circulatory agents are delivered at the interface between the capillaries and the tissue. Removal of carbon dioxide and other waste products also starts here, and then continues through the venules and the veins.

MRI-based perfusion measurement in the brain, assuming an intravascular tracer as in DSC-MRI, enables quantification of three main parameters, i.e. cerebral blood volume (CBV), cerebral blood flow (CBF) and mean transit time (MTT). The relationship between these parameters is defined through the central volume theorem, i.e.:

$$\mathrm{CBV} = \mathrm{CBF} \cdot \mathrm{MTT} \tag{3.1}$$

CBV is defined as the volume of blood per unit mass of tissue and CBF refers to the total volume of blood flow (volume per time) in the capillaries per unit mass of tissue. MTT is the average time an element of blood spends within the capillary system. In the healthy brain, where the cerebral perfusion pressure is normal, CBF and CBV are

correlated by the arteriolar ability to dilate and contract and thus maintain a constant MTT. This condition ensures there is a constant delivery of nutrients to the brain tissue. If the perfusion pressure falls, the arterioles dilate and flow is maintained because of a decrease in vascular resistance. Both CBV and MTT are then increased, while the oxygen extraction remains constant. For larger drops in the perfusion pressure, this condition can no longer be maintained and CBF decreases. The oxygen extraction fraction is then increased instead, to maintain the metabolic rate of oxygen needed for survival. However, for extreme drops in perfusion pressure, cerebral hypoxia or infarction may occur as a result of a failure in the compensatory mechanisms.

Measurements of the above-mentioned parameters are important in the characterization and diagnosis of patients with failures in cerebral haemodynamics, for example, in stroke diagnostics. Reference values are often taken from PET studies such as Leenders et al. (97), where CBF values of 55 ml/(min 100g) and 22 ml/(min 100g) were observed in normal grey and white matter, respectively. In the same study CBV was 5.2 ml/100g and 2.7 ml/100g in grey and white matter, respectively, and MTT is then expected to be 5.7 s in grey matter and 7.3 s in white matter, according to the central volume theorem.

3.2 Intravoxel Incoherent Motion (IVIM)

Intravoxel incoherent motion is a dMRI method, proposed by Le Bihan et al. in the 1980s (9, 33), for obtaining information about the microcirculation and microvasculature in addition to the diffusion parameters. The term IVIM refers to microscopic translational movements of water molecules, caused primarily by both diffusion and perfusion, as well as incoherent flows such as the one caused by CSF, and maybe also the glymphatic system. The perfusion fraction (f_b) is a parameter derived from the IVIM model. In Figure 4, a map of f_b in a healthy volunteer is presented.

In brain applications, perfusion imaging has shown to be particularly important in the medical investigations of stroke and tumours, and IVIM has shown its potential as a diagnostic tool in these areas. The perfusion fraction was significantly decreased in the infarcted area of stroke patients, when compared to the contralateral hemisphere (10-13, 98).

In oncology, gliomas account for 70% of the primary malignant tumours in the adult brain (99). According to the WHO classification, high-grade gliomas are distinguished from low-grade through their density of microvasculature. High-grade gliomas have a disordered network structure with irregular and leaky vessels (100). IVIM imaging has shown an augmented perfusion fraction in high-grade gliomas

compared to what is measured in low-grade gliomas (101-103). Furthermore, patients with an increased perfusion fraction in glioblastoma were found to have a reduced survival rate (104, 105), which suggests IVIM as a valuable method in the prognosis of these patients. The second most common brain tumour is lymphoma, which accounts for 3-5% of primary brain tumours (99). These neoplasms are characterized by a low perfusion due to their densely packed immune cells. This has been confirmed by a significant decrease in the perfusion fraction, when compared to normal brain parenchyma in lymphoma patients (106, 107).

Yet another application of IVIM in the brain is a change in perfusion occurring in the microvasculature following small vessel disease (108-110). Lack of perfusion in brain dead patients has also been confirmed with IVIM (111), as well as perfusion changes in hypercapnia (112) and during visual stimulation (113).

In body imaging, IVIM for perfusion measurement has gained special interest in organs where the capillary blood fraction is high and in tumours, e.g. kidney (114-117), pancreas (118-121), liver (122-126), heart (127, 128), placenta (129), ovarian masses (130), breast (131), prostate (132), and muscles (133).

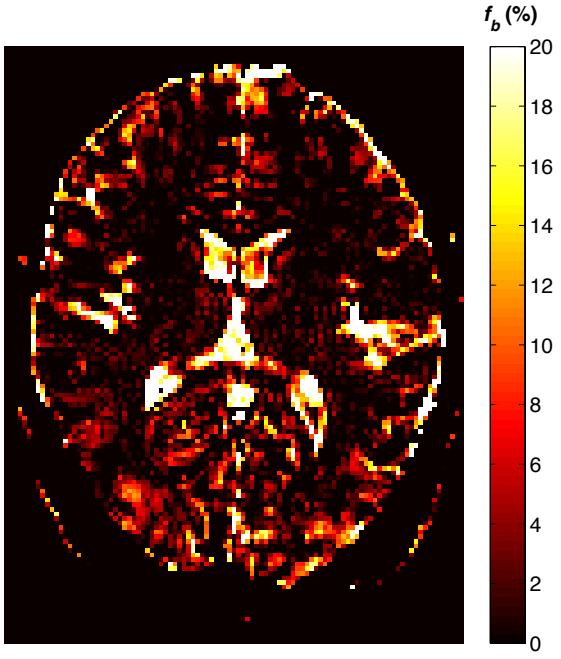

Figure 4. A map of the fractional volumes of blood, f_b (in the range between 0 and 20%), retrievd from a IVIM analysis on data from Paper III. Non-zero f_b values are seen in both GM and WM, but also, erroneously, in large parts of the CSF space.

3.2.1 Background and Principles

The signal reduction in an MR image, caused by the translational molecular movement, increases with the displacement at which the molecules move through a magnetic field gradient. The idea behind IVIM is that blood water moving in the pseudo-randomly oriented capillaries imitates the random walk of diffusing water molecules but on a larger scale. The signal from the microvasculature is thus attenuated in the presence of the motion-encoding gradients in a diffusion sequence, and the pseudo-diffusion coefficient, D^*, then represents the moving blood water molecules in the pseudo-randomly oriented capillary network, often attributed to the perfusion, in each voxel.

In a conventional PGSE experiment, the movement of blood in the microvasculature causes dephasing of blood magnetization in the low b-value regime and the original two-compartment IVIM relationship for this is given by:

$$S = S_0 \left((1 - f_b) e^{-bD} + f_b e^{-b(D+D^*)} \right) \quad (3.2)$$

where S and S_0 are the signal intensities with and without diffusion weighting, respectively, f_b is the perfusion fraction, i.e. the normalized fractional signal of water moving within the capillaries, and (1-f) is the normalized fraction of signal from the tissue. The pseudo-diffusion coefficient, D^*, which carries information about the speed of the blood, is known to be a noise-sensitive parameter and difficult to estimate accurately. Special attention is needed when trying to estimate D^* in a region where the perfusion is very small or vanishing fast, such as in ischemic stroke (13). As pointed out above, the fraction of the voxel that consists of perfused capillaries is generally rather low in cerebral tissue, resulting in a demand for high-SNR IVIM imaging methods.

There are a few parameters that need to be considered and optimized to acquire useful data for IVIM perfusion imaging. Multiple b-value images (usually 10-30) are required, in the interval between 0 and 1000 s/mm^2 (134) since the measured signal at larger b-values can be influenced by non-Gaussian diffusion restrictions, i.e. causing less signal attenuation (135). Also, b=0 s/mm^2 is generally not recommended to include in the fitting due to interactions with the imaging gradient pulses that can affect the results of the IVIM and diffusion analyses (134).

Optimal distributions of b-values have been studied, primarily for abdominal organs and prostate (136, 137). For each b-value the signal is measured in at least three directions, and then averaged to avoid directional dependence.

Even if a protocol with optimized parameters is used for acquiring IVIM data, there are still issues to bear in mind, especially in the brain where the blood volume is as low as 2-5 % (138). According to Paper II, as well as a previous paper on the same topic (139), there is a correlation between low SNR and overestimated perfusion fractions. One way to address this would be scanning in higher field strengths, where

the SNR is expected to be higher. In our study, however, unexpectedly low SNR was observed in the low *b*-value region in grey matter at 7 T, and the relaxation-corrected CBV (cCBV) values at this field strength were also highly overestimated. Loss of signal due to rapid T2 relaxation is also an issue when considering higher field strengths, stressing the importance of SNR-increasing approaches for the IVIM experiment. For example, it is important to keep TE as short as possible to reduce relaxation-induced signal loss. The importance of averaging the IVIM data has also recently been studied, for the purpose of increasing the SNR (140).

The IVIM model fitting can be carried out with various methods, and it is important to keep in mind that the estimated parameters may depend on the fitting algorithm used. Increasing the dimensionality, i.e., the number of model parameters, generally decreases the accuracy of the model fitting, since it becomes sensitive to noise and also becomes ill-posed in the sense that there is more than one set of parameters that may fit the same data. Also if one compartment is very small, the fit may become unstable. Thus, since the IVIM model is multi-exponential, the fitting strategy should be chosen cautiously. One way to increase the robustness of the fitting is to divide it into multiple steps, usually two steps in the IVIM case: one for perfusion parameters and one for diffusion parameters (98, 112, 141), and the optimal way to do this has been investigated (131). The issue with the steps approach is to decide the threshold between the *b*-value interval representing combined diffusion and perfusion effects and the interval that represents pure diffusion. This depends on the tissue of interest, but in the brain, a threshold of 200-400 s/mm^2 is common, even if perfusion can impinge *b*-values up to 600 s/mm^2 (134). Other fitting procedures have been suggested to increase the quality of the fit, such as Bayesian estimation approaches (139, 142), total variation methods (143) and fusion bootstrap moves (98, 144). Since previous studies have reported the benefit of using Bayesian approaches for IVIM analysis (139, 145), we used it in Paper II and Paper III. Although it is advantageous to use Bayesian approaches for data with low SNR (139), it requires extensive computation time and the choice of prior distributions is important (146). In Paper IV, a non-linear least squares algorithm was instead used to fit the model to the signal data.

3.2.2 Validation of the IVIM Method in the Brain

There has been a controversy for a long time concerning whether IVIM is reliable for brain applications (147, 148). The IVIM method was first validated in a phantom consisting of a chromatographic column packed with resin microspheres, 80 μm in diameter (9). Protons inside the microspheres only moved through a diffusion process, while those present in between the spheres moved by gravity and were assumed to flow in random orientations. When the water flowing through the resin was reduced, the measured ADC and perfusion fraction were also decreased,

indicating that the signal obtained with DW-MRI is sensitive to incoherent flow. Later, a number of other phantom studies were performed to evaluate the perfusion dependence of f_b and D^* (149-152).

The IVIM method has also been validated *in vivo* with rat brains by assuring a correlation between the perfusion-related IVIM parameters and the CBF. For example, ^{19}F NMR detectable perfluorocarbons were used as blood substitutes (153). The perfluorocarbons act as a marker for the intravascular compartment since they remain in the intravascular space. It was shown that the diffusion coefficient of the perfluorocarbons measured in live animals was considerably larger than that of freely diffusing perfluorocarbon detected post mortem. IVIM parameters measured in animals also correlated positively with the measured levels of the arterial partial pressure of carbon dioxide pCO_2 (154), which in turn is known to correlate to CBF.

When the signal only originated from the intravascular compartment, the decay of the intravascular ^{19}F signal was still found to be non-monoexponential. In one study, it was proposed that the non-monoexponential behaviour could prove the limitation of the IVIM-model (155), whereas in another investigation this signal behaviour was attributed to the presence of two different vascular components, one arterial and one venous (156). In the latter study, the fast decay was attributed to the arterial component and the venous signal was shown to have a pseudo-diffusion coefficient similar to the diffusion coefficient of tissue.

In pancreas, where the perfusion fraction is expected to be higher than in the brain, blood suppressing inversion has been used to validate the IVIM method (120).

Perfusion-related parameters obtained by the IVIM concept have also been compared with CBV and CBF retrieved by DSC-MRI (157). The results from the IVIM analysis agreed reasonably well with DSC-MRI measures of CBV and CBF.

In contrast to these findings, other animal IVIM studies in the brain could not detect any difference in the perfusion related parameters between dead and alive subjects (158, 159). When CSF was suppressed with an inversion pulse, the biexponential behaviour was also suppressed, and this led to the conclusion that partial volumes of CSF is responsible for at least part of the fast decay compartment (160). It is therefore important to separate the CSF from the blood compartment for accurate perfusion-related IVIM estimates (Paper III).

Another interesting validation study of the IVIM signal origin within the vascular tree suggests that the signal does not only reflect the microvascular compartment, but also originates from larger vessels. The conclusion from that study was that the single vascular compartment assumed in the IVIM model might be an oversimplification (161).

3.2.3 The Link to Classical Perfusion

If assumptions about the topography of the capillary network are made, conventional quantitative measures of perfusion can be estimated from an IVIM experiment (96, 147, 157). Since the perfusion fraction, f_b, is the ratio between the MR visible water volume in the capillaries and the total voxel volume, the relationship between f_b and CBV (in ml/100g) is given by

$$\mathrm{CBV} = 100 \cdot f_b \cdot F_w/\rho \tag{3.3}$$

where F_w is the MR-visible water content fraction of tissue and ρ is the tissue density. This IVIM-based CBV assessment may be of special interest since ASL can not estimate CBV, and IVIM and ASL could therefore complement each other to yield a more complete non-invasive description of the haemodynamics.

If $<l>$ is the average capillary segment length and $<v>$ the average velocity of the blood, the pseudo-perfusion coefficient, D^*, can be expressed as $(<l><v>)/6$. If L is the total capillary length, MTT can be expressed as

$$\mathrm{MTT} = L/<v> = L/(6D^*/<l>) \tag{3.4}$$

Using the central volume theorem (CBF=CBV/MTT), CBF (in ml/(min 100g)) can be approximated as

$$\mathrm{CBF} = 100 \cdot f_b \cdot F_w \cdot 6D^*/(\rho \cdot L \cdot <l>) \tag{3.5}$$

Since both l and L are difficult to assess, absolute quantification of CBF is challenging to achieve. Instead, only a general description of CBF is often aimed for, and the product of f and D^* is frequently used as an approximation to relative CBF.

The relationships in Equations 3.3-3.5 are based on the assumption that the water molecules in blood change velocity several times during the motion encoding, as in Equation 3.1. It should be noted that for short encoding times, the microvascular blood flow may need to be described differently (162).

3.2.4 The Three-Compartment IVIM/Free Water Model

CSF has long been known to bias the IVIM method and the estimation of the perfusion fraction (160). Blood and CSF show similar signal decays (33), since CSF has a large diffusion coeffiecient and additional bulk motion due to cardiac pulsations. Therefore it is difficult to distinguish CSF from blood in voxels with CSF partial volumes. The partial volume effect is especially seen in the cortical grey matter/sulcal interface where CSF and grey matter are often present in the same voxels. One way to remove contamination from CSF is by using an inversion recovery

or T2-prep sequence where CSF is suppressed (160, 163), but for an already SNR sensitive method this is not an optimal solution since the overall SNR is reduced in this approach. A better option for supressing CSF in IVIM imaging, without loosing too much SNR, is to use IR only for b=0 and 1000 s/mm^2 (164). Another proposed way to remove CSF contamination on the estimation of f_b is to remove voxels with heavy TE-dependent voxels assumed to contain CSF (165). However, this method tends to exclude most of the GM tissue. One could also mask the f_b-images by only considering values in between 0 and 0.3 to avoid physiologically irrelevant data (13).

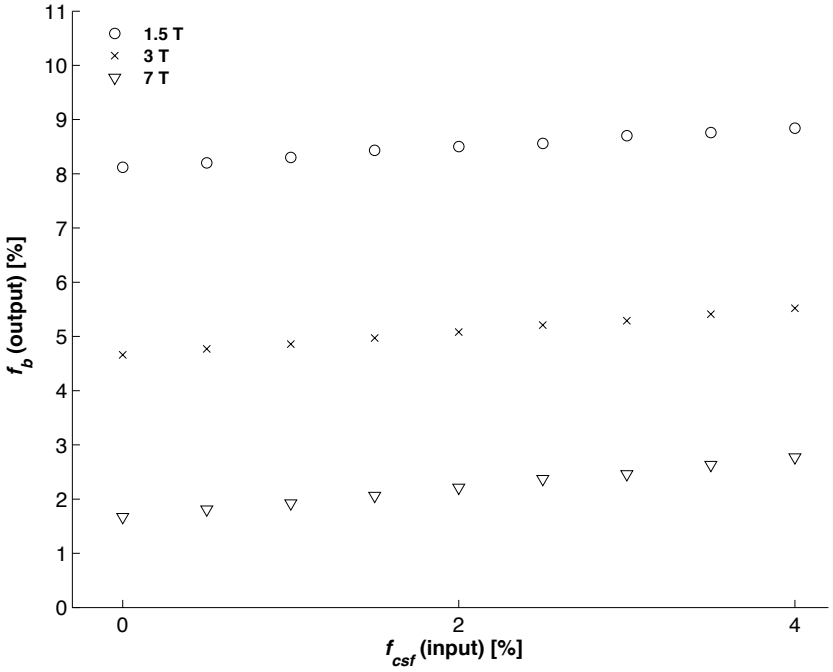

Figure 5. This plot is shown to highlight the effect of CSF on the estimated blood fraction, using a simulation of the effect of the voxel fraction of CSF, f_{CSF}, on the estimated blood fraction, f_b (Paper II).

Hence, in brain tissue, neither the IVIM model (Equation 3.2) nor the free water model (Equation 2.8) constitutes a complete description of the voxel signal because blood and free water/CSF are known to bias each other. We suggested a model that simultaneously accounts for all these components, i.e. tissue, blood and free water (Paper IV). The combination of Equation 2.8 and 3.1 then becomes

$$S_i = S_0 \left[f_b \cdot e^{-b_i D_f} + f_w \cdot e^{-b_i D_w} + (1 - f_b - f_w) \cdot e^{-b_i \boldsymbol{g}_i^T \boldsymbol{D_t} g_i} \right] \qquad (3.6)$$

It is of considerable clinical importance to distinguish between these different compartments since each may reflect different pathologies. It would be particularly interesting to separate effects arising in the extracellular space from those arising in the vascular space.

Using the three-compartment model above, instead of the two-compartment model in Equation 2.8, considerably reduced the bias on f_b to negligible values (Paper IV).

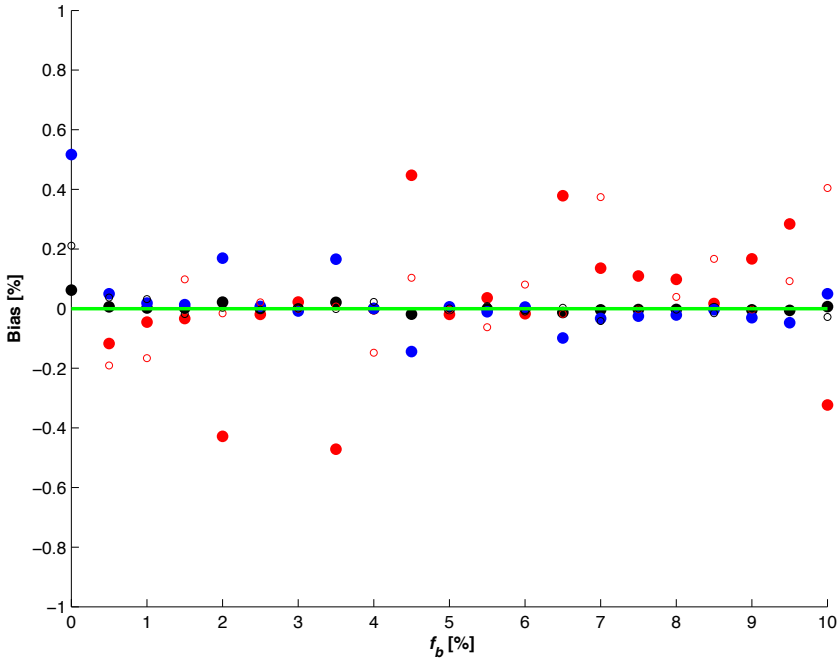

Figure 6. The bias in the f_w estimation when a three-compartment model is used (from Fig 1d in Paper IV), to be compared with Figure 3 (in chapter 2.5).

In vivo results from a healthy volunteer indicated that f_w was reduced to values below 10% in many white matter regions when this three-compartment model was used (Paper IV), which is in good agreement with previous studies of the extracellular volume (166). The fornix was previously known to show an overestimation of the estimated f_w value (167), but when the perfusion effect was accounted for, a reduction of about 30-50% was seen in this area.

In Paper III we also used a three-compartment model to account for the CSF compartment. A significant reduction in the estimated f_b was observed when this

model was used compared to a conventional two-compartment model, suggesting its ability to reduce CSF partial volume effects (Figure 7).

Previous studies with three-compartment models to describe the IVIM signal have been used in brain and prostate cancer (168-170), but the third compartment was dedicated to the slow restricted diffusion attenuation measured at high b-values. Three-compartment models have also been suggested for IVIM in liver (171), where the physiology is different from the brain. None of these suggested three-compartment models incorporated tensor representation to account for anisotropic compartments.

3.2.5 The Extended IVIM Model: Relaxation Compensation

Differences in relaxation properties of the compartments included in a model (usually tissue and blood) are often neglected in conventional IVIM experiments. However, if the compartments have significantly different relaxation properties, the estimated parameters would then be dependent on which TE and repetition time (TR) are used in the imaging sequence. In a study by Lemke et al. (120), this effect was seen in the estimated perfusion fraction, f_b, of pancreatic tissue; f_b was increased as the TE was prolonged due to the difference in relaxation times between the blood and the surrounding pancreatic tissue. The conventional IVIM model (Equation 3.1) was modified to account for these differences according to

$$\frac{S}{S_0} = \frac{(1-f)\cdot\left(1-e^{-\mathrm{TR}/\mathrm{T1}_t}\right)\cdot e^{-\mathrm{TE}/\mathrm{T2}_t - bD} + f\cdot(1-e^{-\mathrm{TR}/\mathrm{T1}_b})\cdot e^{-\mathrm{TE}/\mathrm{T2}_b - b(D+D^*)}}{(1-f)\cdot e^{-\mathrm{TE}/\mathrm{T2}_t}\cdot\left(1-e^{-\mathrm{TR}/\mathrm{T1}_t}\right) + f\cdot e^{-\mathrm{TE}/\mathrm{T2}_b}\cdot(1-e^{-\mathrm{TR}/\mathrm{T1}_b})} \qquad (3.7)$$

where T1 and T2 are the longitudinal and the transversal relaxation times, respectively (t=tissue and b=blood). When this equation was used in combination with literature relaxation time values, the estimated perfusion fraction was close to identical for different echo times.

In the study described in Paper II, where the IVIM method was investigated at different field strengths, similar relaxation compensation was used to account for relaxation differences. In our approach, each signal component (arterial blood=ab and venous blood=vb, GM/WM=t and CSF) was weighted with a factor C_i to compensate for their specific relaxation properties and proton densities (PD), i.e.:

$$C_i = e^{-\mathrm{TE}/\mathrm{T2}_i}\cdot\left(1-e^{-(\mathrm{TR}-\mathrm{TE}/2)/\mathrm{T1}_i}\right)\cdot \mathrm{PD}_i \qquad (3.8)$$

When introducing these weighting factors in Equation 3.2, a corrected CBV (cCBV) was obtained. The cCBV is then given by

$$\mathrm{cCBV} = \frac{f_b(C_t/C_b)}{1-f(1-C_t/C_b)} \tag{3.9}$$

where C_b is the weighted mean of C_{ab} and C_{vb}, and C_t is the weighted mean of $C_{GM/WM}$ and C_{CSF}. The cCBV should give a more adequate representation of the blood volume when results from different field strengths are compared. It is especially important at ultrahigh field strength, e.g. at 7 T, where the T2 for blood, especially the venous part, is very short (Paper II). Although these corrected values should be more reasonable than non-corrected, the noise difference at different field strengths still makes a comparison between them complicated.

Another attempt to improve the analysis is by using both incorporation of relaxation properties in the model and by using a three-component model. This was done in Paper III, where combined knowledge from the studies reported in Paper II and Paper IV was further developed. In this project, the following three-compartment relaxation-compensated IVIM model was used:

$$S = S_{000} \sum_i f_i \rho_i \left[1 - (1-\cos\theta)e^{-\mathrm{TI}/\mathrm{T1}_i} + \left(1 - 2e^{\mathrm{TE}/2\mathrm{T1}_i}\right)\cos\theta\, e^{-\mathrm{TR}/\mathrm{T1}_i}\right] e^{-\mathrm{TE}/\mathrm{T2}_i} e^{-bD_i} \tag{3.10}$$

where i denotes the respective compartment, i.e. i=[tissue(t),CSF(c),blood(b)], S_{000} is the non-weighted (b=0, TE=0, TR=∞) signal value, f_i are the fractional volumes, ρ_i are the water contents, D_i are the diffusion coefficients and θ is the inversion flip angle (assumed to be 180°). Note that D_i=D_b+D^* for i=b. The estimated parameters were then compared to the conventional bi-exponential IVIM model (Equation 3.2), both with and without relaxation compensation.

One important finding from the study described in Paper III is that when relaxation compensation is included in the two-compartment model, a slightly higher precision in the estimation of parameters is observed. When going one step further, i.e. a three-compartment model with relaxation compensation, a better separation between blood and CSF was accomplished. Interestingly, the step from a two-compartment to a three-compartment model seems to have a larger impact on the estimated f_b than the effect of adding relaxation compensation to the two-compartment model, especially in the GM where the highest partial volume of CSF is expected (Figure 7).

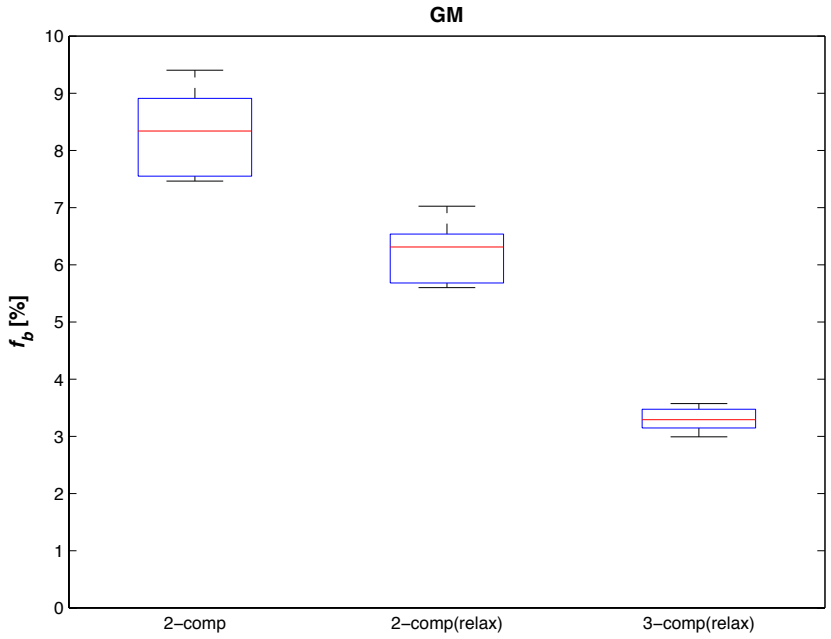

Figure 7. Boxplot of f_b in GM showing the decrease in f_b when going from a two-compartment model to a two-compartment model with relaxation compensation, and, finally, to a three-compartment model with relaxation compensation. Mean f_b in GM is reduced from a mean of 8.3 % to 6.2 %, and to 3.3 %, for the different models specified on the x-axis. The red line represents the median value, the bottom and top edges of the blue box indicate the 25th and 75th percentiles, and the black lines show the entire range of values. Data come from the five volunteers reported in Paper III.

4. Concluding Remarks and Future Aspects

In the projects described in this thesis, estimation approaches for diffusion and perfusion parameters have been explored with the aim to better understand and describe different small-scale features measured with MRI. The Focus was on size estimation on a scale smaller than the actual voxel size itself, as well as on the modelling of signal data from different compartments.

Studying the *q*-space method for estimation of microstructural sizes provided robust agreement with microscopy data in relatively large pores found in an asparagus. A clinical scanner was successfully utilized, despite the violation of the SGP condition and the long diffusion time limit. However, taking this method one step further, for example, for estimation of distribution of axon diameters, other methods such as the ones mentioned in chapter 2.2.1 are likely to be more advantageous as they allow for assessment of smaller sizes.

The IVIM method for estimation of perfusion-related parameters has been investigated and developed. This thesis reports the implications of using ultrahigh field strength MRI to obtain IVIM data, concluding that estimating the blood fraction may be biased in 7 T, likely due to issues related to the increase in field strength, such as the loss of signal from venous blood, and the increased effect of physiological noise. The thesis provides demonstrations that care should be taken in dealing with the CSF in the IVIM data processing. A conclusion is that a three-compartment model where the CSF compartment is included is an effective way for eliminating CSF related bias. However, increasing the number of compartments complicates the fitting procedure, and we proposed several options for stabilizing this fit, such as optimized acquisition schemes and Bayesian approaches. Further efforts to stabilize multiple compartment fits are needed, and another consideration may be suppressing the CSF signal in the acquisition itself.

Nevertheless, a model based approach, such as the three-compartment model proposed in this thesis, has great potential, since it can separate and simultaneously estimate the blood and free water components. Therefore, such models could help in gaining more knowledge about diseases in which it is unclear whether changes are in the vascular or the extracellular space, or both.

The projects reported in this thesis are leading to interesting future aspects. Importantly, the IVIM models developed in this dissertation are now ready for the

application on larger populations, either healthy subjects or patients with altered perfusion or free water distributions. It would also be interesting to translate the relaxation related experiments by, for example, optimizing the acquisition by shortening it and making it a more clinical feasible experiment. Future work could also aim at exploring the potential advantages of using free waveforms in an IVIM measurement, where flow encoding is optimized. Tensor analysis of the IVIM signal could also be of interest in exploring the anisotropy/morphology of the microcirculation (90, 172). Taken together, this thesis sets the ground for future studies, while supporting the use of diffusion MRI and IVIM as unique and clinically important imaging contrast.

Acknowledgements

First and foremost, I would like to thank my main supervisor, Linda Knutsson, for all the support and encouragement and the positive learning environment you have provided during these years. You have given me a lot of scientific assistance, but most of all the freedom to develop my own creativity in all projects. I really appreciate the opportunities you have given me to work with amazing scientists, both in Lund and worldwide. You have always cared about me as a whole person, and we have had a lot of fun!

My co-supervisors, Ronnie Wirestam and Freddy Ståhlberg, thank you so much for your expert advice and support throughout these difficult projects. Your knowledge and solid experience in this field has always been helpful.

I would also like to show my gratitude to all my co-authors. André Ahlgren, I thank you immensely for your scientific support, creative recommendations and solutions to all kinds of problems. You have always made work exciting. Emelie Lind, thank you for all your support, both as a friend and as a colleague. Markus Nilsson, Jimmy Lätt and Sara Brockstedt, is was you and your enthusiasm that started my interest and curiosity in this field.

Filip Szczepankiewicz, I cannot thank you enough for being an amazing and intelligent colleague and co-author, always offering constructive criticism and support. With you as one of my very best friends and officemate it was always fun at work. The only pain you give me is in my stomach when you make me laugh.

To my co-author Matthias J.P. van Osch: your support in deliberating over the problems and findings we had was enlightening and indispensable. A thanks goes to you, and to the staff at the C. J. Gorter Center for High Field MRI in Leiden.

I am also very grateful to my collaborators at the Departments of Psychiatry and Radiology in Boston. Special thanks to Ofer Pasternak, without your help and expertise this would have been impossible, and absolutely not as fun as you made it. You are an amazing colleague who always inspires me. Mahalo nui loa, and hundreds of huli huli to you!

The MR-physics group, the colleagues at the department of Medical Radiation Physics, and the staff at the MR department, you were all very important and this would not have been possible without your assistance and collaboration.

My friends and family, thanks for your support and patience in this journey of mine. There are so many of you, and you have all contributed by being the best friends anyone could ever ask for. Jonas, I'm eternally grateful for your help and for being the best dad to our daughters. Your support was worth more than I can express on paper. Domo arigato.

Last but most importantly, my daughters Majken and Olivia, you are true joy spreaders and the most inspirational people in my world.

References

1. High WA, Ayers RA, Chandler J, Zito G, Cowper SE. Gadolinium is detectable within the tissue of patients with nephrogenic systemic fibrosis. Journal of the American Academy of Dermatology. 2007;56(1):21-6.
2. Franco J. Intracranial deposition of intravenous gadolinium contrast: a literature review. Radiologic Technology. 2017;88(4):435-9.
3. Errante Y, Cirimele V, Mallio CA, Di Lazzaro V, Zobel BB, Quattrocchi CC. Progressive increase of T1 signal intensity of the dentate nucleus on unenhanced magnetic resonance images is associated with cumulative doses of intravenously administered gadodiamide in patients with normal renal function, suggesting dechelation. Investigative Radiology. 2014;49(10):685-90.
4. Kanda T, Ishii K, Kawaguchi H, Kitajima K, Takenaka D. High signal intensity in the dentate nucleus and globus pallidus on unenhanced T1-weighted MR images: relationship with increasing cumulative dose of a gadolinium-based contrast material. Radiology. 2013;270(3):834-41.
5. McDonald RJ, McDonald JS, Kallmes DF, Jentoft ME, Murray DL, Thielen KR, et al. Intracranial gadolinium deposition after contrast-enhanced MR imaging. Radiology. 2015;275(3):772-82.
6. Robert P, Lehericy S, Grand S, Violas X, Fretellier N, Idée J-M, et al. T1-weighted hypersignal in the deep cerebellar nuclei after repeated administrations of gadolinium-based contrast agents in healthy rats: Difference between linear and macrocyclic agents. Investigative Radiology. 2015;50(8):473.
7. Einstein A. Investigations on the Theory of the Brownian Movement. New York: Dover Publications; 1956.
8. Waxman SG, Kocsis JD, Stys PK. The Axon: Structure, Function, and Pathophysiology: Oxford University Press, USA; 1995.
9. Le Bihan D, Breton E, Lallemand D, Aubin ML, Vignaud J, Laval-Jeantet M. Separation of diffusion and perfusion in intravoxel incoherent motion MR imaging. Radiology. 1988;168:497.
10. Yao Y, Zhang S, Tang X, Shi J, Zhu W. Intravoxel incoherent motion diffusion-weighted imaging in stroke patients: Initial clinical experience. Clinical Radiology. 2016;71(9):938. e11-. e16.
11. Suo S, Cao M, Zhu W, Li L, Li J, Shen F, et al. Stroke assessment with intravoxel incoherent motion diffusion-weighted MRI. NMR in Biomedicine. 2016;29(3):320-8.

12. Wirestam R, Brockstedt S, Lindgren A, Geijer B, Thomsen C, Holtås S, et al. The perfusion fraction in volunteers and in patients with ischaemic stroke. Acta Radiologica. 1997;38(6):961-4.
13. Federau C, Sumer S, Becce F, Maeder P, O'Brien K, Meuli R, et al. Intravoxel incoherent motion perfusion imaging in acute stroke: Initial clinical experience. Neuroradiology. 2014;56(8):629-35.
14. Pasternak O, Sochen N, Gur Y, Intrator N, Assaf Y. Free water elimination and mapping from diffusion MRI. Magnetic Resonance in Medicine. 2009;62(3):717-30.
15. Pierpaoli C, Jones D. Removing CSF contamination in brain DT-MRIs by using a two-compartment tensor model. Proceedings of the 12th Annual Meeting of ISMRM. 2004.
16. Metzler-Baddeley C, O'Sullivan MJ, Bells S, Pasternak O, Jones DK. How and how not to correct for CSF-contamination in diffusion MRI. NeuroImage. 2012;59(2):1394-403.
17. Pasternak O, Westin C-F, Bouix S, Seidman LJ, Goldstein JM, Woo T-UW, et al. Excessive extracellular volume reveals a neurodegenerative pattern in schizophrenia onset. The Journal of Neuroscience. 2012;32(48):17365-72.
18. Pasternak O, Kubicki M, Shenton ME. In vivo imaging of neuroinflammation in schizophrenia. Schizophrenia Research. 2016;173(3):200-12.
19. Maier-Hein KH, Westin CF, Shenton ME, Weiner MW, Raj A, Thomann P, et al. Widespread white matter degeneration preceding the onset of dementia. Alzheimer's & Dementia. 2015;11(5):485-93.e2.
20. Ofori E, Pasternak O, Planetta PJ, Li H, Burciu RG, Snyder AF, et al. Longitudinal changes in free-water within the substantia nigra of Parkinson's disease. Brain. 2015;138(8):2322-31.
21. Pasternak O, Koerte IK, Bouix S, Fredman E, Sasaki T, Mayinger M, et al. Hockey Concussion Education Project, Part 2. Microstructural white matter alterations in acutely concussed ice hockey players: A longitudinal free-water MRI study. Journal of Neurosurgery. 2014;120(4):873-81.
22. Crank J. The mathematics of diffusion: Oxford University Press; 1979.
23. Hahn EL. Spin echoes. Physical Review. 1950;80(4):580.
24. Torrey HC. Bloch equations with diffusion terms. Physical review. 1956;104(3):563.
25. Mintorovitch J, Moseley ME, Chileuitt L, Shimizu H, Cohen Y, Weinstein PR. Comparison of diffusion- and T2-weighted MRI for the early detection of cerebral ischemia and reperfusion in rats. Magnetic Resonance in Medicine. 1991;18(1):39-50.
26. Moseley M, Cohen Y, Mintorovitch J, Chileuitt L, Shimizu H, Kucharczyk J, et al. Early detection of regional cerebral ischemia in cats: Comparison of diffusion-and T2-weighted MRI and spectroscopy. Magnetic Resonance in Medicine. 1990;14(2):330-46.
27. Stejskal EO, Tanner JE. Spin diffusion measurements: spin-echo in the presence of a time dependent field gradient. The Journal of Chemical Physics. 1965;42:288.
28. Stejskal E. Use of spin echoes in a pulsed magnetic-field gradient to study anisotropic, restricted diffusion and flow. The Journal of Chemical Physics. 1965;43(10):3597-603.

29. Le Bihan D. Looking into the functional architecture of the brain with diffusion MRI. Nature Reviews Neuroscience. 2003;4(6):469-80.

30. Mattiello J, Basser PJ, Le Bihan D. The b matrix in diffusion tensor echo-planar imaging. Magnetic Resonance in Medicine. 1997;37(2):292-300.

31. Lundell H, Alexander DC, Dyrby TB. High angular resolution diffusion imaging with stimulated echoes: compensation and correction in experiment design and analysis. NMR in Biomedicine. 2014;27(8):918-25.

32. Callaghan PT, MacGowan D, Packer KJ, Zelaya FO. High-resolution q-space imaging in porous structures. Journal of Magnetic Resonance (1969). 1990;90(1):177-82.

33. Le Bihan D, Breton E, Lallemand D, Grenier P, Cabanis E, Laval-Jeantet M. MR imaging of intravoxel incoherent motions: application to diffusion and perfusion in neurologic disorders. Radiology. 1986;161:401.

34. Yablonskiy DA, Sukstanskii AL. Theoretical models of the diffusion weighted MR signal. NMR in Biomedicine. 2010;23(7):661-81.

35. Price WS. Pulsed-field gradient nuclear magnetic resonance as a tool for studying translational diffusion: Part 1. Basic theory. Concepts in Magnetic Resonance. 1997;9(5):299-336.

36. Mitra PP, Halperin BI. Effects of finite gradient-pulse widths in pulsed-field-gradient diffusion measurements. Journal of Magnetic Resonance, Series A. 1995;113(1):94-101.

37. Cory D. Measurement of translational displacement probabilities by NMR: an indicator of compartmentation. Magnetic Resonance in Medicine. 1990;14(3):435-44.

38. Callaghan PT, Coy A. Diffraction-like effects in NMR diffusion studies of fluids in porous solids. Nature. 1991;351(6326):467.

39. Snaar JEM, Hills BP. Constant gradient stimulated echo studies of diffusion in porous materials at high spectrometer fields. Magnetic Resonance Imaging. 1997;15(8):983-92.

40. Assaf Y, Mayk A, Cohen Y. Displacement imaging of spinal cord using q-space diffusion-weighted MRI. Magnetic Resonance in Medicine. 2000;44(5):713-22.

41. Assaf Y, Mayzel-Oreg O, Gigi A, Ben-Bashat D, Mordohovitch M, Verchovsky R, et al. High b value q-space-analyzed diffusion MRI in vascular dementia: A preliminary study. Journal of the Neurological Sciences. 2002;203:235-9.

42. Assaf Y, Ben-Bashat D, Chapman J, Peled S, Biton I, Kafri M, et al. High b-value q-space analyzed diffusion-weighted MRI: Application to multiple sclerosis. Magnetic Resonance in Medicine. 2002;47(1):115-26.

43. Ben Bashat D, Kronfeld-Duenias V, Zachor DA, Ekstein PM, Hendler T, Tarrasch R, et al. Accelerated maturation of white matter in young children with autism: A high b value DWI study. NeuroImage. 2007;37(1):40-7.

44. Hoffmeister B, Jänig W, Lisney S. A proposed relationship between circumference and conduction velocity of unmyelinated axons from normal and regenerated cat hindlimb cutaneous nerves. Neuroscience. 1991;42(2):603-11.

45. Horowitz A, Barazany D, Tavor I, Bernstein M, Yovel G, Assaf Y. In vivo correlation between axon diameter and conduction velocity in the human brain. Brain Structure and Function. 2015;220(3):1777-88.

46. Boujraf Sd, Luypaert R, Eisendrath H, Osteaux M. Echo planar magnetic resonance imaging of anisotropic diffusion in asparagus stems. Magnetic Resonance Materials in Physics, Biology and Medicine. 2001;13(2):82-90.

47. Topgaard D, Söderman O. Experimental determination of pore shape and size using q-space NMR microscopy in the long diffusion-time limit. Magnetic Resonance Imaging. 2003;21(1):69-76.

48. Peled S, Cory DG, Raymond SA, Kirschner DA, Jolesz FA. Water diffusion, T2, and compartmentation in frog sciatic nerve. Magnetic Resonance in Medicine. 1999;42(5):911.

49. Avram L, Assaf Y, Cohen Y. The effect of rotational angle and experimental parameters on the diffraction patterns and micro-structural information obtained from q-space diffusion NMR: Implication for diffusion in white matter fibers. Journal of Magnetic Resonance. 2004;169(1):30-8.

50. Malmborg C, Topgaard D, Söderman O. NMR diffusometry and the short gradient pulse limit approximation. Journal of Magnetic Resonance. 2004;169(1):85-91.

51. Bar-Shir A, Avram L, Özarslan E, Basser PJ, Cohen Y. The effect of the diffusion time and pulse gradient duration ratio on the diffraction pattern and the structural information estimated from q-space diffusion MR: Experiments and simulations. Journal of Magnetic Resonance. 2008;194(2):230-6.

52. Lätt J, Nilsson M, Malmborg C, Rosquist H, Wirestam R, Ståhlberg F, et al. Accuracy of q-space related parameters in MRI: Simulations and phantom measurements. IEEE Transactions on Medical Imaging. 2007;26(11):1437-47.

53. Ong HH, Wright AC, Wehrli SL, Souza A, Schwartz ED, Hwang SN, et al. Indirect measurement of regional axon diameter in excised mouse spinal cord with q-space imaging: simulation and experimental studies. NeuroImage. 2008;40(4):1619-32.

54. Cohen Y, Assaf Y. High b-value q-space analyzed diffusion-weighted MRS and MRI in neuronal tissues – a technical review. NMR in Biomedicine. 2002;15(7-8):516-42.

55. Assaf Y, Blumenfeld-Katzir T, Yovel Y, Basser PJ. AxCaliber: a method for measuring axon diameter distribution from diffusion MRI. Magnetic Resonance in Medicine. 2008;59(6):1347-54.

56. Alexander DC, Hubbard PL, Hall MG, Moore EA, Ptito M, Parker GJ, et al. Orientationally invariant indices of axon diameter and density from diffusion MRI. NeuroImage. 2010;52(4):1374-89.

57. Schachter M, Does MD, Anderson AW, Gore JC. Measurements of restricted diffusion using an oscillating gradient spin-echo sequence. Journal of Magnetic Resonance. 2000;147(2):232-7.

58. Martin M. Measuring restriction sizes using diffusion weighted magnetic resonance Imaging: A Review. Magnetic Resonance Insights. 2013;6:59-64.

59. Xu J, Li H, Harkins KD, Jiang X, Xie J, Kang H, et al. Mapping mean axon diameter and axonal volume fraction by MRI using temporal diffusion spectroscopy. NeuroImage. 2014;103:10-9.

60. Hansen JR. Pulsed NMR study of water mobility in muscle and brain tissue. Biochimica et Biophysica Acta (BBA)-General Subjects. 1971;230(3):482-6.

61. Cleveland G, Chang D, Hazlewood C, Rorschach H. Nuclear magnetic resonance measurement of skeletal muscle: anisotrophy of the diffusion coefficient of the intracellular water. Biophysical Journal. 1976;16(9):1043-53.

62. Chenevert TL, Brunberg JA, Pipe JG. Anisotropic diffusion in human white matter: demonstration with MR techniques in vivo. Radiology. 1990;177(2):401-5.

63. Alexander AL, Lee JE, Lazar M, Field AS. Diffusion tensor imaging of the brain. Neurotherapeutics: the Journal of the American Society for Experimental NeuroTherapeutics. 2007;4(3):316-29.

64. Basser PJ, Mattiello J, LeBihan D. MR diffusion tensor spectroscopy and imaging. Biophysical Journal. 1994;66(1):259-67.

65. Pierpaoli C, Basser PJ. Toward a quantitative assessment of diffusion anisotropy. Magnetic Resonance in Medicine. 1996;36(6):893-906.

66. Basser PJ, Mattiello J, Lebihan D. Estimation of the Effective Self-Diffusion Tensor from the NMR Spin Echo. Journal of Magnetic Resonance, Series B. 1994;103(3):247-54.

67. Pierpaoli C, Jezzard P, Basser PJ, Barnett A, Di Chiro G. Diffusion tensor MR imaging of the human brain. Radiology. 1996;201(3):637-48.

68. Basser PJ, Jones DK. Diffusion-tensor MRI: theory, experimental design and data analysis–a technical review. NMR in Biomedicine. 2002;15(7-8):456-67.

69. Papadopoulos M, Saadoun S, Binder D, Manley G, Krishna S, Verkman A. Molecular mechanisms of brain tumor edema. Neuroscience. 2004;129(4):1009-18.

70. Unterberg A, Stover J, Kress B, Kiening K. Edema and brain trauma. Neuroscience. 2004;129(4):1019-27.

71. Alexander AL, Hasan KM, Lazar M, Tsuruda JS, Parker DL. Analysis of partial volume effects in diffusion-tensor MRI. Magnetic Resonance in Medicine. 2001;45(5):770-80.

72. Papadakis NG, Martin KM, Mustafa MH, Wilkinson ID, Griffiths PD, Huang CLH, et al. Study of the effect of CSF suppression on white matter diffusion anisotropy mapping of healthy human brain. Magnetic Resonance in Medicine. 2002;48(2):394-8.

73. Chou M-C, Lin Y-R, Huang T-Y, Wang C-Y, Chung H-W, Juan C-J, et al. FLAIR diffusion-tensor MR tractography: comparison of fiber tracking with conventional imaging. American Journal of Neuroradiology. 2005;26(3):591-7.

74. Concha L, Gross DW, Beaulieu C. Diffusion tensor tractography of the limbic system. American Journal of Neuroradiology. 2005;26(9):2267-74.

75. Cercignani M, Inglese M, Pagani E, Comi G, Filippi M. Mean diffusivity and fractional anisotropy histograms of patients with multiple sclerosis. American Journal of Neuroradiology. 2001;22(5):952-8.

76. Assaf Y, Pasternak O. Diffusion tensor imaging (DTI)-based white matter mapping in brain research: a review. Journal of Molecular Neuroscience. 2008;34(1):51-61.

77. Schonberg T, Pianka P, Hendler T, Pasternak O, Assaf Y. Characterization of displaced white matter by brain tumors using combined DTI and fMRI. NeuroImage. 2006;30(4):1100-11.

78. Pierpaoli C, Marenco S, Rohde G, Jones D, Barnett A. Analyzing the contribution of cardiac pulsation to the variability of quantities derived from the diffusion tensor. Proceedings of the 11th Annual Meeting of ISMRM. 2003.

79. Pasternak O, Shenton ME, Westin C-F. Estimation of Extracellular Volume from Regularized Multi-shell Diffusion MRI. In: Ayache N, Delingette H, Golland P, Mori K, editors. Medical Image Computing and Computer-Assisted Intervention – MICCAI 2012: 15th International Conference, Nice, France, October 1-5, 2012, Proceedings, Part II. Berlin, Heidelberg: Springer Berlin Heidelberg; 2012. p. 305-12.

80. Hoy AR, Koay CG, Kecskemeti SR, Alexander AL. Optimization of a free water elimination two-compartment model for diffusion tensor imaging. NeuroImage. 2014;103:323-33.

81. Pasternak O, Assaf Y, Intrator N, Sochen N. Variational multiple-tensor fitting of fiber-ambiguous diffusion-weighted magnetic resonance imaging voxels. Magnetic Resonance Imaging. 2008;26(8):1133-44.

82. Zhang H, Schneider T, Wheeler-Kingshott CA, Alexander DC. NODDI: Practical in vivo neurite orientation dispersion and density imaging of the human brain. NeuroImage. 2012;61(4):1000-16.

83. Barazany D, Basser PJ, Assaf Y. In vivo measurement of axon diameter distribution in the corpus callosum of rat brain. Brain. 2009;132(5):1210-20.

84. Wang Y, Wang Q, Haldar JP, Yeh F-C, Xie M, Sun P, et al. Quantification of increased cellularity during inflammatory demyelination. Brain. 2011;134(12):3587-98.

85. Berlot R, Metzler-Baddeley C, Jones DK, O'Sullivan MJ. CSF contamination contributes to apparent microstructural alterations in mild cognitive impairment. NeuroImage. 2014;92:27-35.

86. Metzler-Baddeley C, Hunt S, Jones DK, Leemans A, Aggleton JP, O'Sullivan MJ. Temporal association tracts and the breakdown of episodic memory in mild cognitive impairment. Neurology. 2012;79(23):2233-40.

87. Bergamino M, Pasternak O, Farmer M, Shenton ME, Paul Hamilton J. Applying a free-water correction to diffusion imaging data uncovers stress-related neural pathology in depression. NeuroImage: Clinical. 2016;10:336-42.

88. Padhani AR, Liu G, Mu-Koh D, Chenevert TL, Thoeny HC, Takahara T, et al. Diffusion-weighted magnetic resonance imaging as a cancer biomarker: Consensus and recommendations. Neoplasia. 2009;11(2):102-25.

89. Atlas SW. Magnetic Resonance Imaging of the Brain and Spine. Lippincott Williams & Wilkins; 2009.

90. Tofts PS. Modeling tracer kinetics in dynamic Gd-DTPA MR imaging. Journal of Magnetic Resonance Imaging. 1997;7(1):91-101.

91. Rosen BR, Belliveau JW, Vevea JM, Brady TJ. Perfusion imaging with NMR contrast agents. Magnetic Resonance in Medicine. 1990;14(2):249-65.

92. Williams DS, Detre JA, Leigh JS, Koretsky AP. Magnetic resonance imaging of perfusion using spin inversion of arterial water. Proceedings of the National Academy of Sciences. 1992;89(1):212-6.

93. Golay X, Hendrikse J, Lim TC. Perfusion imaging using arterial spin labeling. Topics in Magnetic Resonance Imaging. 2004;15(1):10-27.

94. Perthen JE, Calamante F, Gadian DG, Connelly A. Is quantification of bolus tracking MRI reliable without deconvolution? Magnetic Resonance in Medicine. 2002;47(1):61-7.

95. Wintermark M, Sesay M, Barbier E, Borbély K, Dillon WP, Eastwood JD, et al. Comparative overview of brain perfusion imaging techniques. Stroke. 2005;36(9):e83-e99.

96. Bihan DL, Turner R. The capillary network: a link between IVIM and classical perfusion. Magnetic Resonance in Medicine. 1992;27(1):171-8.

97. Leenders K, Perani D, Lammertsma A, Heather J, Buckingham P, Jones T, et al. Cerebral blood flow, blood volume and oxygen utilization: Normal values and effect of age. Brain. 1990;113(1):27-47.

98. Federau C, O'Brien K, Meuli R, Hagmann P, Maeder P. Measuring brain perfusion with intravoxel incoherent motion (IVIM): Initial clinical experience. Journal of Magnetic Resonance Imaging. 2014;39(3):624-32.

99. Ricard D, Idbaih A, Ducray F, Lahutte M, Hoang-Xuan K, Delattre J-Y. Primary brain tumours in adults. The Lancet. 2012;379(9830):1984-96.

100. Pries AR, Höpfner M, Le Noble F, Dewhirst MW, Secomb TW. The shunt problem: control of functional shunting in normal and tumour vasculature. Nature Reviews Cancer. 2010;10(8):587.

101. Bisdas S, San Koh T, Roder C, Braun C, Schittenhelm J, Ernemann U, et al. Intravoxel incoherent motion diffusion-weighted MR imaging of gliomas: feasibility of the method and initial results. Neuroradiology. 2013;55(10):1189-96.

102. Federau C, Meuli R, O'Brien K, Maeder P, Hagmann P. Perfusion measurement in brain gliomas with intravoxel incoherent motion MRI. American Journal of Neuroradiology. 2014;35(2):256-62.

103. Togao O, Hiwatashi A, Yamashita K, Kikuchi K, Mizoguchi M, Yoshimoto K, et al. Differentiation of high-grade and low-grade diffuse gliomas by intravoxel incoherent motion MR imaging. Neuro-Oncology. 2016;18(1):132-41.

104. Puig J, Sánchez-González J, Blasco G, Daunis-i-Estadella P, Federau C, Alberich-Bayarri Á, et al. Intravoxel incoherent motion metrics as potential biomarkers for survival in glioblastoma. PloS one. 2016;11(7):e0158887.

105. Federau C, Cerny M, Roux M, Mosimann PJ, Maeder P, Meuli R, et al. IVIM perfusion fraction is prognostic for survival in brain glioma. Clinical Neuroradiology. 2016:1-8.

106. Suh CH, Kim HS, Lee SS, Kim N, Yoon HM, Choi C-G, et al. Atypical imaging features of primary central nervous system lymphoma that mimics glioblastoma: utility of intravoxel incoherent motion MR imaging. Radiology. 2014;272(2):504-13.

107. Yamashita K, Hiwatashi A, Togao O, Kikuchi K, Kitamura Y, Mizoguchi M, et al. Diagnostic utility of intravoxel incoherent motion MR imaging in differentiating primary central nervous system lymphoma from glioblastoma multiforme. Journal of Magnetic Resonance Imaging. 2016;44(5):1256-61.

108. Wong SM, Zhang CE, van Bussel FC, Staals J, Jeukens CR, Hofman PA, et al. Simultaneous investigation of microvasculature and parenchyma in cerebral small vessel disease using intravoxel incoherent motion imaging. NeuroImage: Clinical. 2017;14:216-21.

109. Zhang CE, Wong SM, Uiterwijk R, Staals J, Backes WH, Hoff EI, et al. Intravoxel incoherent motion imaging in small vessel disease. Stroke. 2017;48(3):658-63.

110. Sun J, Yu X, Jiaerken Y, Song R, Huang P, Wang C, et al. The relationship between microvasculature in white matter hyperintensities and cognitive function. Brain Imaging and Behavior. 2017;11(2):503-11.

111. Federau C, Nguyen A, Christensen S, Saba L, Wintermark M. Cerebral perfusion measurement in brain death with intravoxel incoherent motion imaging. Neurovascular Imaging. 2016;2(1):9.

112. Federau C, Maeder P, O'Brien K, Browaeys P, Meuli R, Hagmann P. Quantitative measurement of brain perfusion with intravoxel incoherent motion MR imaging. Radiology. 2012;265(3):874-81.

113. Federau C, O'Brien K, Birbaumer A, Meuli R, Hagmann P, Maeder P. Functional mapping of the human visual cortex with intravoxel incoherent motion MRI. PLoS One. 2015;10(2):e0117706.

114. Sigmund EE, Vivier P-H, Sui D, Lamparello NA, Tantillo K, Mikheev A, et al. Intravoxel incoherent motion and diffusion-tensor imaging in renal tissue under hydration and furosemide flow challenges. Radiology. 2012;263(3):758-69.

115. Chandarana H, Kang SK, Wong S, Rusinek H, Zhang JL, Arizono S, et al. Diffusion-weighted intravoxel incoherent motion imaging of renal tumors with histopathologic correlation. Investigative Radiology. 2012;47(12):688-96.

116. Tsuda K, Murakami T, Sakurai K, Harada K, Kim T, Takahashi S, et al. Preliminary evaluation of the apparent diffusion coefficient of the kidney with a spiral IVIM sequence. Nihon Igaku Hoshasen Gakkai zasshi Nippon Acta Radiologica. 1997;57(1):19-22.

117. Powers TA, Lorenz CH, Holburn GE, Price RR. Renal artery stenosis: in vivo perfusion MR imaging. Radiology. 1991;178:543.

118. Kang KM, Lee JM, Yoon JH, Kiefer B, Han JK, Choi BI. Intravoxel incoherent motion diffusion-weighted MR imaging for characterization of focal pancreatic lesions. Radiology. 2014;270(2):444-53.

119. Re TJ, Lemke A, Klauss M, Laun FB, Simon D, Grünberg K, et al. Enhancing pancreatic adenocarcinoma delineation in diffusion derived intravoxel incoherent motion f-maps through automatic vessel and duct segmentation. Magnetic Resonance in Medicine. 2011;66(5):1327-32.

120. Lemke A, Laun FB, Simon D, Stieltjes B, Schad LR. An in vivo verification of the intravoxel incoherent motion effect in diffusion-weighted imaging of the abdomen. Magn Resonance in Medicine. 2010;64:1580.

121. Lemke A, Laun FB, Klau M. Differentiation of pancreas carcinoma from healthy pancreatic tissue using multiple b-values: Comparison of apparent diffusion coefficient and intravoxel incoherent motion derived parameters. Investigative Radiology. 2009;44:769.

122. Joo I, Lee JM, Han JK, Choi BI. Intravoxel incoherent motion diffusion-weighted MR imaging for monitoring the therapeutic efficacy of the vascular disrupting agent CKD-516 in rabbit VX2 liver tumors. Radiology. 2014;272(2):417-26.

123. Chow AM, Gao DS, Fan SJ, Qiao Z, Lee FY, Yang J, et al. Liver fibrosis: an intravoxel incoherent motion (IVIM) study. Journal of Magnetic Resonance Imaging. 2012;36(1):159-67.

124. Guiu B, Petit J-M, Capitan V, Aho S, Masson D, Lefevre P-H, et al. Intravoxel incoherent motion diffusion-weighted imaging in nonalcoholic fatty liver disease: a 3.0-T MR study. Radiology. 2012;265(1):96-103.

125. Luciani A, Vignaud A, Cavet M. Liver cirrhosis: intravoxel incoherent motion MR imaging—pilot study. Radiology. 2008;249:891.

126. Yamada I, Aung W, Himeno Y, Nakagawa T, Shibuya H. Diffusion coefficients in abdominal organs and hepatic lesions: evaluation with intravoxel incoherent motion echo-planar MR imaging. Radiology. 1999;210:617.

127. Moulin K, Croisille P, Feiweier T, Delattre B, Wei H, Robert B, et al. In vivo free-breathing DTI and IVIM of the whole human heart using a real-time slice-followed SE-EPI navigator-based sequence: A reproducibility study in healthy volunteers. Magnetic Resonance in Medicine. 2016;76(1):70-82.

128. Callot V, Bennett E, Decking UK, Balaban RS, Wen H. In vivo study of microcirculation in canine myocardium using the IVIM method. Magnetic Resonance in Medicine. 2003;50(3):531-40.

129. Moore R, Strachan B, Tyler D, Duncan K, Baker P, Worthington B, et al. In utero perfusing fraction maps in normal and growth restricted pregnancy measured using IVIM echo-planar MRI. Placenta. 2000;21(7):726-32.

130. Morita S, Kojima S, Hirata M, Suzuki K, Ueno E. Perfusion fraction of diffusion-weighted MRI for predicting the presence of blood supply in ovarian masses. Journal of Magnetic Resonance Imaging. 2011;34(5):1131-6.

131. Suo S, Lin N, Wang H, Zhang L, Wang R, Zhang S, et al. Intravoxel incoherent motion diffusion-weighted MR imaging of breast cancer at 3.0 tesla: Comparison of different curve-fitting methods. Journal of Magnetic Resonance Imaging. 2015;42(2):362-70.

132. Shinmoto H, Tamura C, Soga S, Shiomi E, Yoshihara N, Kaji T, et al. An intravoxel incoherent motion diffusion-weighted imaging study of prostate cancer. American Journal of Roentgenology. 2012;199(4):W496-W500.

133. Nguyen A, Ledoux J-B, Omoumi P, Becce F, Forget J, Federau C. Selective microvascular muscle perfusion imaging in the shoulder with intravoxel incoherent motion (IVIM). Magnetic Resonance Imaging. 2017;35:91-7.

134. Iima M, Le Bihan D. Clinical intravoxel incoherent motion and diffusion MR imaging: past, present, and future. Radiology. 2015;278(1):13-32.

135. Clark CA, Le Bihan D. Water diffusion compartmentation and anisotropy at high b values in the human brain. Magnetic Resonance in Medicine. 2000;44(6):852-9.

136. Lemke A, Stieltjes B, Schad LR, Laun FB. Toward an optimal distribution of b values for intravoxel incoherent motion imaging. Magnetic Resonance Imaging. 2011;29(6):766-76.

137. Pang Y, Turkbey B, Bernardo M, Kruecker J, Kadoury S, Merino MJ, et al. Intravoxel incoherent motion (IVIM) MR imaging for prostate cancer: An evaluation of perfusion fraction and diffusion coefficient derived from different b-value combinations. Magnetic Resonance in Medicine. 2013;69(2):553-62.

138. Pro H, Kanno I, Fukuda H. Human cerebral circulation: positron emission tomography studies. Annals of Nuclear Medicine. 2005;19(2):65-74.

139. Neil JJ, Bretthorst GL. On the use of Bayesian probability theory for analysis of exponential decay data: an example taken from intravoxel incoherent motion experiments. Magnetic Resonance in Medicine. 1993;29:642.

140. Merisaari H, Federau C. Quantitative noise analysis for increased homogeneity in intra-voxel incoherent motion (IVIM) perfusion imaging in brain. Proceedings of the 25th ISMRM meeting. 2017.

141. Iima M, Reynaud O, Tsurugizawa T, Ciobanu L, Li J-R, Geffroy F, et al. Characterization of glioma microcirculation and tissue features using intravoxel incoherent motion magnetic resonance imaging in a rat brain model. Investigative Radiology. 2014;49(7):485-90.

142. Orton MR, Collins DJ, Koh D-M, Leach MO. Improved intravoxel incoherent motion analysis of diffusion weighted imaging by data driven Bayesian modeling. Magnetic Resonance in Medicine. 2014;71(1):411-20.

143. Lin C, Shih Y-Y, Huang S-L, Huang H-M. Total variation-based method for generation of intravoxel incoherent motion parametric images in MRI. Magnetic Resonance in Medicine. 2017;78(4):1383-91.

144. Freiman M, Perez-Rossello JM, Callahan MJ, Voss SD, Ecklund K, Mulkern RV, et al. Reliable estimation of incoherent motion parametric maps from diffusion-weighted MRI using fusion bootstrap moves. Medical Image Analysis. 2013;17(3):325-36.

145. Barbieri S, Donati OF, Froehlich JM, Thoeny HC. Impact of the calculation algorithm on biexponential fitting of diffusion-weighted MRI in upper abdominal organs. Magnetic Resonance in Medicine. 2016;75(5):2175-84.

146. Gustafsson O, Montelius M, Starck G, Ljungberg M. Impact of prior distributions and central tendency measures on Bayesian intravoxel incoherent motion model fitting. Magnetic Resonance in Medicine. 2017:n/a-n/a.

147. Henkelman RM. Does IVIM measure classical perfusion? Magnetic Resonance in Medicine. 1990;16:470.

148. Bisdas S. Are we ready to image the incoherent molecular motion in our minds? Neuroradiology. 2013;55(5):537-40.

149. Lee JH, Cheong H, Lee SS, Lee CK, Sung YS, Huh J-W, et al. Perfusion assessment using intravoxel incoherent motion-based analysis of diffusion-weighted magnetic resonance imaging: validation through phantom experiments. Investigative Radiology. 2016;51(8):520-8.

150. Cho GY, Kim S, Jensen JH, Storey P, Sodickson DK, Sigmund EE. A versatile flow phantom for intravoxel incoherent motion MRI. Magnetic Resonance in Medicine. 2012;67(6):1710-20.

151. Lorenz CH, Pickens DR, Puffer DB, Price RR. Magnetic resonance diffusion/perfusion phantom experiments. Magnetic Resonance in Medicine. 1991;19(2):254-60.

152. Turner R, Le Bihan D, Maier J, Vavrek R, Hedges LK, Pekar J. Echo-planar imaging of intravoxel incoherent motion. Radiology. 1990;177(2):407-14.

153. Neil JJ, Ackerman JJ. Detection of pseudodiffusion in rat brain following blood substitution with perfluorocarbon. Journal of Magnetic Resonance (1969). 1992;97(1):194-201.

154. Neil JJ, Bosch CS, Ackerman JJ. An evaluation of the sensitivity of the intravoxel incoherent motion (IVIM) method of blood flow measurement to changes in cerebral blood flow. Magnetic Resonance in Medicine. 1994;32:60.

155. Henkelman RM, Neil JJ, Xiang QS. A quantitative interpretation of IVIM measurements of vascular perfusion in the rat brain. Magnetic Resonance in Medicine. 1994;32:464.

156. Duong TQ, Kim SG. In vivo MR measurements of regional arterial and venous blood volume fractions in intact rat brain. Magnetic Resonance in Medicine. 2000;43(3):393-402.

157. Wirestam R, Borg M, Brockstedt S, Lindgren A, Holtas S, Stahlberg F. Perfusion-related parameters in intravoxel incoherent motion MR imaging compared with CBV and CBF measured by dynamic susceptibility-contrast MR technique. Acta Radiologica. 2001;42:123.

158. MacFall J, Maki J, Johnson G, Hedlund L, Benveniste H, Copher G. Diffusion/microcirculation MRI in the rat brain. Magnetic Resonance in Medicine. 1991;19(2):305-10.

159. McKinstry RC, Weiskoff RM, Belliveau JW, Vevea JM, Moore JB, Kwong KW, et al. Ultrafast MR imaging of water mobility: animal models of altered cerebral perfusion. Journal of Magnetic Resonance Imaging. 1992;2(4):377-84.

160. Kwong K, McKinstry R, Chien D, Crawley A, Pearlman J, Rosen B. CSF-suppressed quantitative single-shot diffusion imaging. Magnetic Resonance in Medicine. 1991;21(1):157-63.

161. Zhang X, Ingo C, Teeuwisse WM, Chen Z, van Osch MJP. Comparison of perfusion signal acquired by arterial spin labeling–prepared intravoxel incoherent motion (IVIM)

MRI and conventional IVIM MRI to unravel the origin of the IVIM signal. Magnetic Resonance in Medicine.n/a-n/a.

162. Ahlgren A, Knutsson L, Wirestam R, Nilsson M, Ståhlberg F, Topgaard D, et al. Quantification of microcirculatory parameters by joint analysis of flow-compensated and non-flow-compensated intravoxel incoherent motion (IVIM) data. NMR in Biomedicine. 2016;29(5):640-9.
163. Federau C, O'Brien K. Increased brain perfusion contrast with T2-prepared intravoxel incoherent motion (T2prep IVIM) MRI. NMR in Biomedicine. 2015;28(1):9-16.
164. Tamura H, Mugikura S, Komori Y, Yamanaka K, Ota H. Estimation and removal of partial volume effects of cerebrospinal fluid in intravoxel incoherent motion (IVIM) imaging. Proceedings of the 23rd ISMRM meeting. 2015
165. Bisdas S, Klose U. IVIM analysis of brain tumors: an investigation of the relaxation effects of CSF, blood, and tumor tissue on the estimated perfusion fraction. Magnetic Resonance Materials in Physics, Biology and Medicine. 2015;28(4):377-83.
166. Syková E, Nicholson C. Diffusion in Brain Extracellular Space. Physiological Reviews. 2008;88(4):1277.
167. De Santis S, Drakesmith M, Bells S, Assaf Y, Jones DK. Why diffusion tensor MRI does well only some of the time: Variance and covariance of white matter tissue microstructure attributes in the living human brain. NeuroImage. 2014;89:35-44.
168. Ohno N, Miyati T, Kobayashi S, Gabata T. Modified triexponential analysis of intravoxel incoherent motion for brain perfusion and diffusion. Journal of Magnetic Resonance Imaging. 2016;43(4):818-23.
169. Ueda Y, Takahashi S, Ohno N, Kyotani K, Kawamitu H, Miyati T, et al. Triexponential function analysis of diffusion-weighted MRI for diagnosing prostate cancer. Journal of Magnetic Resonance Imaging. 2016;43(1):138-48.
170. Nicolas R, Sibon I, Hiba B. Accuracies and contrasts of models of the diffusion-weighted-dependent attenuation of the MRI signal at intermediate b-values. Magnetic Resonance Insights. 2015;8:11.
171. Cercueil J-P, Petit J-M, Nougaret S, Soyer P, Fohlen A, Pierredon-Foulongne M-A, et al. Intravoxel incoherent motion diffusion-weighted imaging in the liver: Comparison of mono-, bi- and tri-exponential modelling at 3.0-T. European Radiology. 2015;25(6):1541-50.
172. Finkenstaedt T, Klarhoefer M, Eberhardt C, Becker AS, Andreisek G, Boss A, et al. The IVIM signal in the healthy cerebral gray matter: A play of spherical and non-spherical components. NeuroImage. 2017;152:340-7.